

METAL-ORGANIC FRAMEWORK/GRAPHENE OXIDE DERIVED POROUS  
CARBONS FOR PLATINUM BASED ELECTROCATALYSTS FOR OXYGEN  
REDUCTION REACTION

by

EMRE BURAK BOZ

Submitted to the Graduate School of Engineering and Natural Sciences  
in partial fulfillment of  
the requirements for the degree of  
Master of Science

Sabancı University

January 2019

METAL-ORGANIC FRAMEWORK/GRAPHENE OXIDE DERIVED POROUS  
CARBONS FOR PLATINUM BASED ELECTROCATALYSTS FOR OXYGEN  
REDUCTION REACTION

APPROVED BY:

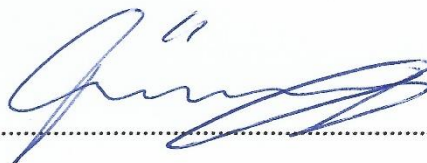
Prof. Dr. Selmiye Alkan Gürsel .....  
(Thesis Supervisor)



Assoc. Prof. Dr. Emre Erdem.....



Assoc. Prof. Dr. Önder Metin.....



DATE OF APPROVAL: 07/01/2019

© Emre Burak Boz 2019

All Rights Reserved

# METAL-ORGANIC FRAMEWORK/GRAPHENE OXIDE DERIVED POROUS CARBONS FOR PLATINUM BASED ELECTROCATALYSTS FOR OXYGEN REDUCTION REACTION

EMRE BURAK BOZ

Materials Science and Nano Engineering, M.Sc. Thesis, 2019

**Thesis Advisor:** Prof. Dr. Selmiye Alkan Gürsel

**Keywords:** metal-organic frameworks, graphene oxide, hierarchically porous materials, electrocatalysis, oxygen reduction reaction

## ABSTRACT

Fossil fuel-based energy economy is bound to change at some point within the 21<sup>st</sup> century as fossil fuels are inherently limited sources. Energy conversion and storage devices such as batteries, fuel cells, solar cells and supercapacitors need to advance in terms of efficiency for the fruition of a renewable energy ecosystem. Hierarchically porous materials are utilized as catalyst supports in polymer electrolyte membrane fuel cells (PEMFCs) and batteries to increase mass transfer and active site density in the catalyst. Metal-organic frameworks (MOFs) are tailorable crystalline solids where organic linker units are connected to metal centers. They may form molecular gates, channels and pores within the framework in angstrom to nanometer scale. Porous carbons derived from metal-organic frameworks are promising catalyst supports owing to their high surface area and 3-D network structure. In this thesis, a porous carbon has been produced from pyrolysis of a hybrid material based on Zn based MOF called zeolitic imidazolate framework-8 (ZIF-8) and graphene oxide (GO). As observed by physical and chemical characterization, ZIF-8 were coordinated to GO during the synthesis conditions of ZIF-8 and formed a hybrid structure in contrast with simple mixing. Evolution of macro/mesoporosity have been observed when the hybrid was exposed to pyrolyzing temperatures owing to the exfoliating effect of GO on ZIF-8. Pt nanoparticle (Pt NP) deposition on this porous carbon has resulted in catalyst Cat-1, which has been tested via voltammetric experiments against two reference materials; Pt decorated on pyrolyzed ZIF-8 (Cat-0) and Pt decorated on reduced GO (Pt/rGO). Cat-1 exhibits increased mass and specific activity against Pt/rGO at 0.8 V for oxygen reduction reaction (ORR). The nature of increased activity is proposed to be increased mass transport properties of Cat-1 sample that originates from its hierarchical porosity.

# METAL-ORGANİK KAFES/GRAFEN OKSİT TÜREVLİ GÖZENEKLİ KARBONLARIN PLATİN BAZLI OKSİJEN İNDİRGENME REAKSİYONU ELEKTROKATALİZÖRLERİNDE KULLANIMI

EMRE BURAK BOZ

Malzeme Bilimi ve Nano Mühendislik, Yüksek Lisans Tezi, 2019

**Tez Danışmanı:** Prof. Dr. Selmiye Alkan Gürsel

**Anahtar Kelimeler:** metal-organik kafes, grafen oksit, hiyerarşik gözenekli malzemeler, elektrokataliz, oksijen indirgenme reaksiyonu

## ÖZET

Fosil yakıtların sınırlı kaynaklar olması fosil yakıtı dayalı enerji ekonomisini 21'inci yüzyılın bir aşamasında değiştirmeye zorlayacak. Yenilenebilir enerji ekosistemine geçiş için bataryalar, yakıt ve güneş pilleri ve süperkapasitörler gibi enerji çevrim ve depolama araçlarının verimliliğinin artırılması gerekiyor. Hiyerarşik gözenekli malzemeler katalizörlerdeki kütle transferi ve aktif bölge yoğunluğunu artırmalarından dolayı polimer elektrolit membranlı (PEM) yakıt pillerinde ve bataryalarda kullanılıyorlar. Metal-organik kafes'ler organik moleküllerin metal merkezler ile bağlanması sonucu oluşan kontrol edilebilir kristal katılardır. Bu yapılar angstrom ve nanometre seviyesinde moleküler kapılar, geçitler ve gözenekler oluşturabilirler. Metal-organik kafeslerden türemiş gözenekli karbonlar yüksek yüzey alanları ve 3-B ağ yapıları nedeniyle umut vaadeden katalizör destekleridirler. Bu tezde Zn esaslı bir MOF olan zeolitik imidazolat kafes-8 (ZIF-8) ve grafen oksit (GO) hibritleşmesi sonucu oluşan yapıya uygulanan piroliz sonucu gözenekli karbon elde edilmiştir. Fiziksel ve kimyasal karakterizasyonlardan da anlaşılacağı üzere, ZIF-8 grafen oksite ZIF-8'in sentez koşulları sırasında koordine olmuş ve basit karışım durumuna zıt olarak bir hibrit yapısı oluşturmuştur. Hibrit piroliz sıcaklıklarına çıkarıldığında GO'nun ZIF-8 üzerindeki pullanma etkisi sayesinde meso/makroporöz bir yapı elde edilmiştir. Hibrit malzeme üzerine Pt nanoparçacık (Pt NP) kaplanması sonucunda üretilen katalizör (Cat-1) iki farklı referans malzeme olan ZIF-8'in pirolizi üzerinde Pt NP kaplanması (Cat-0) ve indirgenmiş GO üzerine Pt NP kaplanması (Pt/rGO) ile voltametrik deneyler sayesinde karşılaştırılmıştır. Cat-1 katalizörünün oksijen indirgenme reaksiyonu (ORR) için 0.8 V'ta kütle aktivitesi ve spesifik aktivite değerleri Pt/rGO'ya göre daha yüksektir. Yüksek

aktivitenin kaynađı olarak Cat-1 katalizöründeki hiyerarşik gözenekli yapının bu katalizördeki kütle transferi özelliklerini yükseltmesi önerilmektedir.

*To my loving family for their infinite support  
and friends who shared this journey with me*

## ACKNOWLEDGEMENTS

I would first like to express my heartfelt gratitude and thanks to my thesis advisor Prof. Dr. Selmiye Alkan Gürsel for fostering me as a scientist and researcher and allowing me to be part of her research group. My jury members Assoc. Prof. Önder Metin and Assoc. Prof. Emre Erdem also deserve special thanks for devoting their time for reading my thesis and attending my thesis defense.

I also would like to thank Sabancı University for providing tuition waiver throughout my graduate studies. It has been my second home for 6 years now and I will always feel a sense of longing towards this place, wherever I may be. I am also thankful of my MAT teachers who expanded my imagination and I aspire to be like them.

I am grateful for the help I received from my mentors and colleagues throughout this study; Dr. Emre Biçer has assisted me with the synthesis of MOFs and piqued my interest on this class of materials in the first place. Adnan Taşdemir for being “the guy” when I needed something; he never shied away from helping me and I will never be able to repay the time he spent for me. I also would like to acknowledge Dr. Alp Yürüm for helping me with BET analysis and his constructive contributions. My group members Navid, Naeimeh, Esaam, Faisal and Buse; I am grateful for all the time we spent in lab and discussions and of course your company.

Most special thanks go to my friends, without them these two years would mean much less to me. My actual roommate Onur Zırhlı, and my honorary roommates Alp Ertunga Eyüpoğlu, Deniz Anıl and Hana Korneti; I will miss every moment we spent with all its ups and downs, I know our paths will cross again. I also would like to thank Murat Tansan for the shared experience of 11 years, Yelda Yorulmaz for leading the way for me and Melih Can Taşdelen for keeping my spirits up. Last but not least, my cousin and friend Deniz Boz deserves a special thanks for being the best cousin ever.

My deepest gratitude goes to my family; they set me up for this path and are a source of endless support and inspiration for me. They always encouraged and helped me to perform at my best and hopefully I won't disappoint them.

## TABLE OF CONTENTS

1. INTRODUCTION .....	1
1.1. Electrochemistry and Fuel Cells.....	1
1.2. Kinetics of ORR .....	4
1.3. Voltammetric Methods for ORR .....	8
1.4. Support Materials for ORR .....	13
1.4.1. Carbon Black.....	13
1.4.2. Carbon Nanotubes .....	14
1.4.3. Graphene & Graphene Oxide.....	16
1.4.4. Hybrid Structures .....	18
1.5. Metal-Organic Framework derived Supports & Catalysts .....	19
1.6. Summary & Motivation.....	24
1.7. Aim & Objectives.....	25
1.8. Novelty .....	25
2. EXPERIMENTAL.....	26
2.1. ZIF-8 and ZIF-8/GO Synthesis .....	26
2.2. Pyrolysis of ZIF-8 and ZIF-8/GO.....	26
2.3. Acid Wash of ZIF-8 and ZIF-8/GO.....	27
2.4. Pt Deposition on Porous Carbons via Polyol Method .....	27
2.5. Characterization.....	28
2.6. Electrochemical Tests of Catalysts.....	28
3. RESULTS AND DISCUSSION.....	31
3.1. GO as a Platform for ZIF-8 Growth .....	31
3.1.1. Chemical perspective .....	31
3.1.2. Crystallographic perspective .....	32
3.1.3. Morphological perspective.....	35
3.1.4. Textural perspective .....	36

3.2. Effect of ZIF-8 and GO on Electrochemical Performance.....	39
4. CONCLUSION.....	51
BIBLIOGRAPHY.....	52

## LIST OF FIGURES

<b>Figure 1.</b> Simple fuel cell scheme.....	1
<b>Figure 2.</b> From bulk solution to electrode surface, oxidation-reduction reactions and the pathway of such system .....	3
<b>Figure 3.</b> Effect of applied potential on fermi level of electrode and charge transfer between electrode and reactant molecule. ....	5
<b>Figure 4.</b> Free energy vs reaction coordinate on Pt(111) surface for ORR .....	7
<b>Figure 5.</b> A textbook CV curve of Pt .....	9
<b>Figure 6.</b> LSV curves for Pt/C catalysts in 3 different films and two scan rates in RDE test.....	11
<b>Figure 7.</b> Deviation from ideal Levich line for a slow reaction.....	12
<b>Figure 8.</b> Pt NPs supported on carbon black (Vulcan) from low to high magnification (a, c, b to d). 2-3 nm sized Pt NPs are visible with poor dispersion on CB.....	14
<b>Figure 9.</b> Pt-Vulcan before (a) and after (b) durability test. Pt-MWCNT before (c) and after (d) durability test .....	15
<b>Figure 10.</b> Wrapping graphene (2D) into fullerenes (0D) or rolling into carbon nanotubes (1D). Stacking layers of graphene makes graphite (3D). ....	17
<b>Figure 11.</b> Catalyst layer with Pt on graphene (a) and Pt on graphene but with a spacer material in between (carbon black in the reference) (b) .....	19
<b>Figure 12.</b> From 1 to 16, IRMOF structures with different organic linkers .....	20
<b>Figure 13.</b> Proposed mechanism for active site generation in Co(Im) <sub>2</sub> MOF. ....	22
<b>Figure 14.</b> Macropores created by fiber network facilitate mass transport and micropores derived from ZIF-8 precursor host catalytically active sites. ....	23
<b>Figure 15.</b> TGA of ZIF-8/GO in N <sub>2</sub> atmosphere.....	27
<b>Figure 16.</b> CV and LSV parameter correction for Ag/AgCl electrode .....	29
<b>Figure 17.</b> FT-IR graph of ZIF-8, GO and ZIF-8 GO from top to bottom can be seen. Important vibrations are affixed. ....	31
<b>Figure 18.</b> Simulated graphene and GO diffractograms (top) and simulated ZIF-8, as prepared ZIF-8 and hybrid ZIF-8/GO diffractograms (bottom). ....	33
<b>Figure 19.</b> Simulated ZnO (a), non-washed NC-0 (b), non-washed NC-1 (c), acid washed NC-0 (d) and acid washed NC-1 (e). ....	34
<b>Figure 20.</b> SEM micrographs of ZIF-8 (a), ZIF-8/GO (b), NC-0 (c), NC-1 (d), Cat-0 (e), Cat-1 (f).....	35

<b>Figure 21.</b> N <sub>2</sub> isotherms of ZIF-8 & NC-0 (a) and ZIF-8/GO & NC-1 (b). In (c) ZIF-8/GO is given with reversed axes to show intake behavior at mid-pressure range. ....	37
<b>Figure 22.</b> BJH pore size distribution of ZIF-8, ZIF-8/GO, NC-0 and NC-1. 2 to 10 nm range can be seen in the inset.....	38
<b>Figure 23.</b> XRD graph of Simulated Pt (a), Cat-0 (b), Cat-1 (c) and Pt/rGO (d). ....	40
<b>Figure 24.</b> Average crystallite sizes of Cat-0, Cat-1 and Pt/rGO with error bars attached (n=4).....	40
<b>Figure 25.</b> TEM images of Pt/rGO (a, b, c) and Cat-0 (d, e, f). Inset of (c) shows average interplanar spacing (111) of Pt NPs in Pt/rGO. ....	42
<b>Figure 26.</b> TEM images of Cat-1 (a), (b), (c) and (d). Inset of (c) shows average interplanar spacing (111) of a Pt NP on Cat-1. HAADF-STEM image of the unusual structure in Cat-1 (e) and its EDX analysis (f). ....	44
<b>Figure 27.</b> CV response of catalysts Cat-0, Cat-1 and Pt/rGO taken in N <sub>2</sub> purged 0.1 M HClO <sub>4</sub> .....	47
<b>Figure 28.</b> LSV scans in O <sub>2</sub> purged 0.1 M HClO <sub>4</sub> of Cat-0, Cat-1 and Pt/rGO.....	48
<b>Figure 29.</b> Mass activity and specific activity values of Cat-1 and Pt/rGO.....	50

## LIST OF TABLES

<b>Table 1.</b> FT-IR stretches of select functional groups in ZIF-8, GO and ZIF-8/GO.....	31
<b>Table 2.</b> Surface area calculation of ZIF-8, ZIF-8/GO, NC-0 and NC-1.....	39
<b>Table 3.</b> Theoretical and TG based Pt amount and ECSA values of Cat-0, Cat-1 and Pt/rGO.....	46

## LIST OF ABBREVIATIONS

FC: Fuel Cell

HOR: Hydrogen Oxidation Reaction

ORR: Oxygen Reduction Reaction

HER: Hydrogen Evolution Reaction

PEMFC: Polymer Electrolyte Membrane Fuel Cell

ADMFC: Alkaline Direct Methanol Fuel Cell

PGM: Platinum Group Metals

NHE: Normal Hydrogen Electrode

RHE: Reversible Hydrogen Electrode

PDS: Potential Determining Step

RDS: Rate Determining Step

DFT: Density Functional Theory

RDE: Rotating Disc Electrode

CV: Cyclic Voltammetry

LSV: Linear Sweep Voltammetry

NP: Nanoparticle

CB: Carbon Black

(MW/SW)CNT: (Multi Wall/Single Wall) Carbon Nanotube

GO: Graphene Oxide

rGO: Reduced Graphene Oxide

MOF: Metal Organic Framework

IRMOF: Isoreticular Metal Organic Framework

ZIF: Zeolitic Imidazolate Framework

MIL: Matériaux de l'Institut Lavoisier

SBU: Secondary Building Unit

XRD: X-Ray Diffraction

SEM: Scanning Electron Microscope

(S)TEM: (Scanning) Transmission Electron Microscope

HAADF: High-Angle Annular Dark Field

EDX: Energy Dispersive X-Ray Spectroscopy

FFT: Fast Fourier Transform

FT-IR: Fourier Transformed-Infrared Spectroscopy

ATR: Attenuated Total Reflectance

TGA: Thermogravimetric Analyzer

DTG: Differential Thermogravimetry

BET: Brunauer-Emmett-Teller

BJH: Barrett-Joyner-Halenda

ECSA / EASA: Electrochemical Surface Area / Electrochemically Active Surface Area

# 1. INTRODUCTION

## 1.1. Electrochemistry and Fuel Cells

Dependence on fossil fuels for energy has brought upon the anthropogenic climate change on us; it is threatening every human being (present and future) indiscriminately and is the major challenge of the century<sup>1</sup>. Shifting towards renewable alternatives is necessary and among renewables, hydrogen brings forth a global paradigm shift in energy economy<sup>2,3</sup>. Hydrogen is the lightest element of the periodic table with energy density (per mass) far surpassing fossil fuels and hydrocarbons. Unlike primary energy sources, hydrogen is not readily available to extract as it is bound in compounds in earth's crust, oceans and atmosphere. Hydrogen could be visualized as a basic energy storage unit which can be generated on site and akin to a battery, store excess electrical energy in chemical form. Utilization of hydrogen for electricity generation, transportation, heating etc. requires efficient storage, transfer and extraction of chemically stored energy; all of them are major engineering problems. Undoubtedly, there are several barriers on the way to global scale hydrogen economy and one of them is efficient energy conversion. Devices that convert chemical energy stored in hydrogen (or a hydrocarbon) and oxygen to electricity are called fuel cells (FCs). FCs operate on the principle of controlled reduction and oxidation reactions, similar to other electrochemical devices such as batteries. Any fuel cell is simply composed of an anode, where hydrogen is oxidized to protons; and cathode, where oxygen is reduced to water. The protons are conducted through an electrolyte in the cell between anode and cathode, but electrons are carried outside, flowing through a wire towards the potential gradient (from anode to cathode) and generating useful work. Basic operation of a fuel cell is depicted in **Figure 1**.

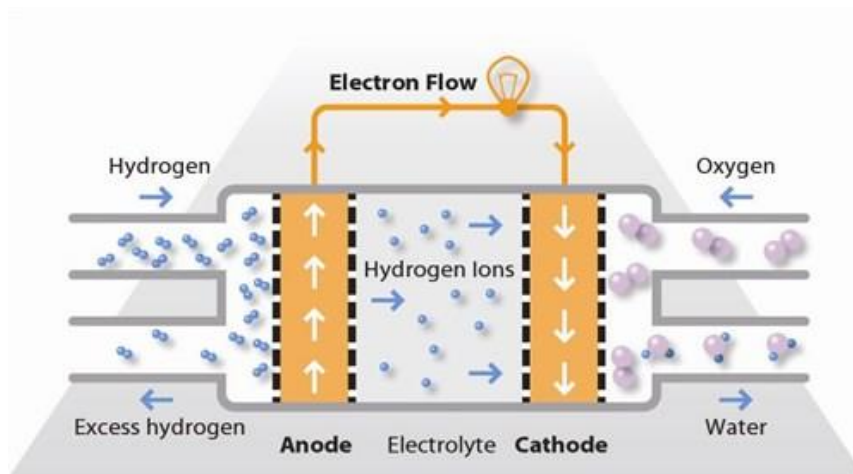
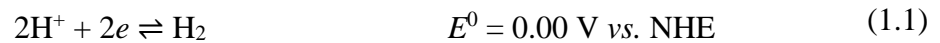


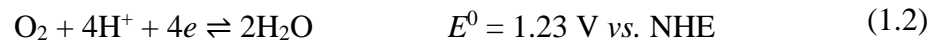
**Figure 1.** Simple fuel cell scheme. Reproduced from FuelCellToday<sup>4</sup>.

From this point onward, readers are assumed to have basic knowledge on physical chemistry and concepts such as standard potential and oxidation-reduction reactions. Readers that wish to learn more about electrochemistry is strongly advised to take a look at ‘Electrochemical Methods: Fundamentals and Applications’ by Allen J. Bard & Larry R. Faulkner.

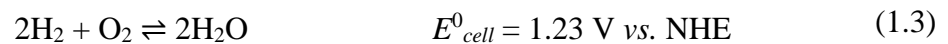
Electrochemical reactions need to take place at anode and cathode so that there is a potential difference created between them, which will move the electrons on the external circuit. Electrons of hydrogen ( $e^-$ ) are stripped off at the anode site and fed to the circuit, and protons ( $H^+$ ) flow towards the cathode. This reaction is called as hydrogen oxidation reaction (HOR) and has a standard potential of 0.00 V versus normal hydrogen electrode (NHE), which is tautological as this is the reaction occurring in a hydrogen electrode. Thus, the anodic half-reaction can be written as;



For the cathode side of the fuel cell, protons coming from anode and electrons that flow through the circuit combine with oxygen to create water. This reaction is called oxygen reduction reaction (ORR) and has a standard potential of +1.23 V versus NHE. The standard potentials are conventionally given as reduction potentials and the positive sign for ORR means that it is spontaneous under standard conditions. The cathodic half-reaction can be written as;



Thus, the overall reaction in a fuel cell can be given as;



This is the equilibrium potential of a fuel cell and does not take concentration of reactants and products or the temperature of the system into consideration. Complete thermodynamic view of an electrochemical cell can be realized by the Nernst equation;

$$E_{cell} = E^0_{cell} - \frac{RT}{nF} \ln Q_r \quad (1.4)$$

where R is universal gas constant, T is temperature, n is the number of electrons transferred in reaction, F is Faraday constant and  $Q_r$  is the reaction quotient written in terms of concentrations (or partial pressures).

The thermodynamic relations, based on Nernst equation, can only tell us if a reaction will move forward or not because they are ultimately dependent on the Gibbs free energy of the electrochemical transformations. The measured potential in a fuel cell (or any electrochemical full cell) will divert from equilibrium potential if system is not in equilibrium, which is the case when there is a net current flowing through. Electrochemical processes such as HOR and ORR are also dependent on reaction rate, which is controlled by mass transfer to electrode, electron transfer, chemical reactions occurring at electrode surface and adsorption-desorption mechanisms<sup>5</sup>. The current flowing through the electrode is controlled by these parameters, which are ultimately dependent on the potential applied. The processes that occur on the surface of a single electrode during a redox reaction is illustrated in **Figure 2**, with electrode, surface region and bulk solution seen from left to right.

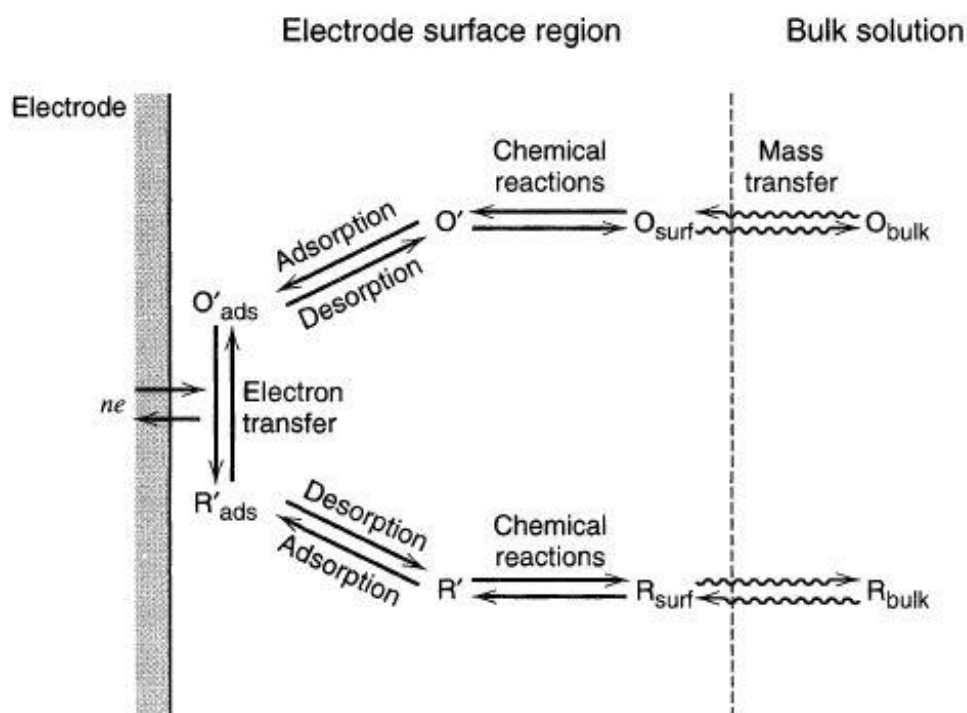
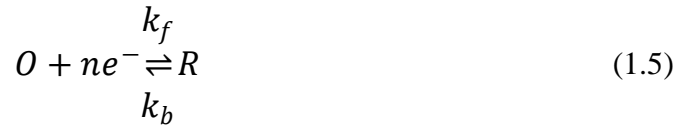


**Figure 2.** From bulk solution to electrode surface, oxidation-reduction reactions and the pathway of such system. Reproduced with permission from John Wiley and Sons, *Electrochemical Methods: Fundamentals and Applications*, Ref<sup>5</sup>, Copyright 2001.

In an actual system all processes contribute to the current, but for the sake of discussion, let's focus on kinetically controlled current. Kinetically controlled means that surface of electrode is focused where electron transfer is carried out. Mass transfer is not considered in this approach. It is possible to incorporate contribution to current density from applied potential and mass transfer as will be revealed in next chapter.

## 1.2. Kinetics of ORR

For a simple reduction reaction in the form of;



the reduction of 'O' to 'R' is designated as the forward reaction and  $k_f$  is the forward reaction rate constant. Since rate of an electrochemical reaction is essentially the number of electrons reacting per time, the fundamental relation between the reaction rate and current can be written as;

$$v = \frac{i}{nFA} \quad [mol\ s^{-1}\ cm^{-2}] \quad (1.6)$$

where  $v$  is the rate of reaction,  $i$  is the current and  $A$  is the electrode area. Rate of a reaction, in a more analytical sense, can also be written in terms of concentration;

$$v_f = k_f C_O(0, t) = \frac{i_c}{nFA} \quad (1.7)$$

where  $C_O(0,t)$  denotes concentration of species 'O' at zero distance from surface of the electrode (meaning surface concentration) at time  $t$ , and  $i_c$  is the cathodic current since this is a reduction reaction. By incorporating backward reaction as well, we can formulize the relation between current and concentration as;

$$i = i_c - i_a = nFA[k_f C_O(0, t) - k_b C_R(0, t)] \quad (1.8)$$

This formula does not take applied potential into consideration and thus will be modified by overpotential contributions. For the reaction given in (1.5), suppose a positive potential  $E$  ( $E > E_0$ ) is applied to the system. This creates an overpotential  $\Delta E$  ( $E - E^0$ ) which drives the system to non-equilibrium condition. Here, **increasing** the potential means **decreasing** the energy of electrons in the electrode, analogous to connecting a battery to the electrode on its positive side. This confusing convention comes from early days of electrical studies where positive charge was thought to be the carrier. Increasing the potential promotes the flow of electrons from the solution to the electrode and will be favorable for oxidation of analyte. An analogous demonstration with fermi

levels of electrode, molecular orbitals of analyte and corresponding changes with respect to applied potential can be found in **Figure 3**. Thus, applied positive potential will shift the barrier for oxidation to a lower value than standard barrier of oxidation for this reaction. Similarly, the reduction barrier will increase.

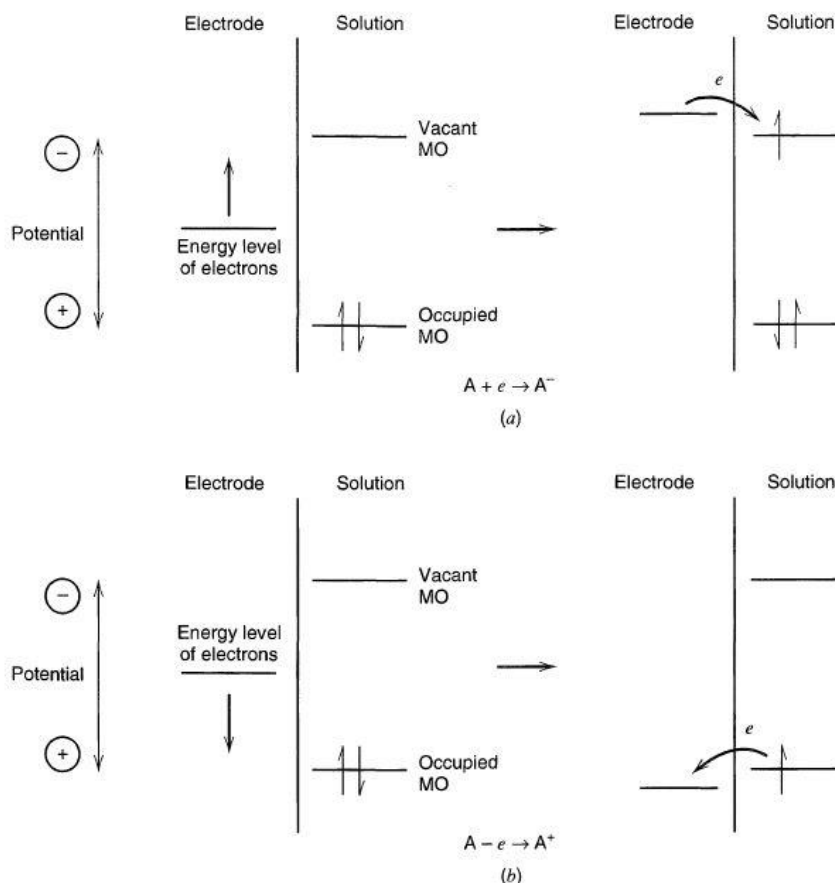


**Figure 3.** Effect of applied potential on fermi level of electrode and charge transfer between electrode and reactant molecule. In (a) decreasing the potential promotes reduction whereas in (b) increased potential promotes oxidation. Reprinted with permission from John Wiley and Sons, *Electrochemical Methods: Fundamentals and Applications*, Ref <sup>5</sup>, Copyright 2001.

If potential of system is raised by  $\Delta E$ , then the energy of electrons on electrode changes by  $-F\Delta E$  (minus indicates reduced energy). This change in energy will modify the standard free energy for oxidation (or anodic barrier) and reduction (cathodic barrier) as;

$$\Delta G_a^* = \Delta G_{0a}^* - (1 - a)F\Delta E \quad \& \quad \Delta G_c^* = \Delta G_{0c}^* + aF\Delta E \quad (1.9)$$

where  $G_0^*$  terms are standard free energy of their respective process and  $a$  is the charge transfer coefficient. The coefficient is necessary as the change in energy doesn't modify

the reduction and oxidation potentials at the same degree. If the rate constants are assumed to obey Arrhenius relation (as most rate constants do);

$$k = A e^{-E_A/RT} \quad (1.10)$$

then by implementing 1.9 into activation energy term ( $E_A$ ) of 1.10 reveals;

$$k_f = A_f \exp\left(\frac{-\Delta G_{0c}^*}{RT}\right) \exp\left[-a\Delta E f\right] \quad (1.11)$$

$$k_b = A_b \exp\left(\frac{-\Delta G_{0a}^*}{RT}\right) \exp\left[(1-a)\Delta E f\right] \quad (1.12)$$

where  $A_x$  terms are Arrhenius constants and  $f$  is equal to  $F/RT$ . Now think of a solution in equilibrium with electrode interface, and the concentration of species 'O' and 'R' is equal to each other in this solution. Remember that initial equilibrium condition meant that the standard barrier of oxidation of species 'R' and reduction of species 'O' were equal to each other. So, this is an equilibrium condition for the solution as well; forward and reverse rate constants and standard energy of activation for oxidation and reduction are equal to each other such that a standard rate constant ( $k_0$ ) can be defined by;

$$k^0 = A_0 \exp\left(\frac{-\Delta G_0^*}{RT}\right) \quad (1.13)$$

When all the rate constants of 1.10 and 1.11 are combined with 1.8, one can formulize current in terms of concentrations and overpotential;

$$i = F A k^0 [C_O(0, t) e^{-af\Delta E} - C_R(0, t) e^{(1-a)f\Delta E}] \quad (1.14)$$

This is the **Butler-Volmer equation** and defines the relationship between applied potential to the system and measured current. It is also possible to envelope Faraday constant, concentration and rate constant terms to come up with a term called exchange current density which is equal to cathodic and anodic current densities under equilibrium conditions. As can be seen from the formula, it is possible to increase the current by increasing the overpotential.

ORR is an inherently sluggish multi-electron reaction. Unlike HOR at the anode, ORR requires high loadings of expensive metals such as Pt and Pt alloys to increase the reaction rate. In ORR catalyzed by Pt, oxygen is believed to be reduced in a multi-step path as shown<sup>6</sup>;



where ‘ad’ denotes adsorbed species on Pt(111) surface. This is also called dissociative mechanism where diatomic oxygen dissociates before adsorbing on the surface. There is also peroxo (associative) mechanism which has oxygen intermediates in the form of  $OOH_{ads}$  but will not be discussed here. As per Sabatier principle, a good catalyst should bind intermediates strong enough to adsorb them in the first place, and weak enough so that final intermediates can dissociate<sup>7</sup>. Although there could be other reasons behind the slow kinetics of ORR, one approach is to study the binding energies of intermediates.

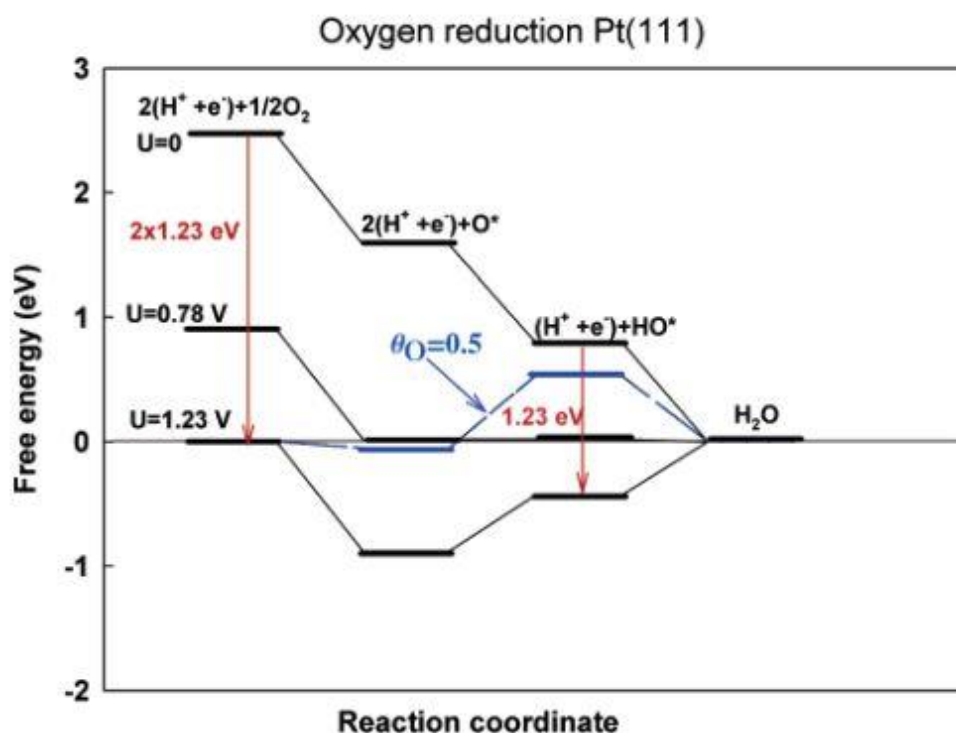


**Figure 4.** Free energy vs reaction coordinate on Pt(111) surface for ORR. Three cell potentials ( $U = 0, 0.78$  and  $1.23$ ) are calculated. Black paths are for low oxygen coverage on surface whereas blue one is for half coverage for  $U = 1.23$  V. Reprinted with permission from The Journal of Physical Chemistry B, Ref<sup>6</sup>. Copyright 2004 American Chemical Society.

At 1.23 V, ORR is at equilibrium potential; this means with overpotential it is possible to drive the reaction towards reduction. That holds true, but the problem is at the magnitude of this overpotential. It is not possible to start ORR without driving the system with at least nearly 0.2 V overpotential. Only then reaction proceeds and significant current is achieved. The same is true for water oxidation reaction in the reverse direction. There are still debates on the origin of this overpotential, but significant work has been done to explain it. Nørskov et al. have studied the thermodynamic equilibrium potentials of reaction intermediates to find the potential determining step (PDS)<sup>6</sup>, which is a reliable way to study catalytic activity.

The rate-determining step (RDS) is the first electron transfer step in ORR, based on examination of Tafel slopes<sup>7</sup>, and is controlled by the PDS (which is the last electron transfer step based on Ref<sup>6</sup>). This is supported by the fact that desorption of OH<sub>ads</sub> species creates empty sites for adsorption of oxygen<sup>8</sup>. Thus, improving the thermodynamics of ORR allows one to improve kinetics of the reaction as well, which does not apply to all heterogenous catalysis<sup>7</sup>.

When the cell potential is at 0.00 V the reaction proceeds as free energy change between consecutive intermediates is downhill. One would expect this trend to continue until 1.23 V cell potential (which is the equilibrium potential) for a reversible reaction with fast kinetics. But as we can see from the DFT calculation in **Figure 4**, the most stable intermediate becomes adsorbed oxygen. This means that high overpotential is necessary to polarize the electrode and destabilize oxygenated species. As these species are thermodynamically difficult to remove from Pt surface, first course of action on Pt based catalysts (at cathode side) should be focused on reducing the bond strength between Pt and oxygen intermediates. Indeed, there are experimental studies on modifying Pt electronic structure by creating intermetallic compounds such as Pt<sub>3</sub>Ni<sup>8</sup> and Pt<sub>3</sub>Y, Pt<sub>3</sub>Sc<sup>9</sup> that demonstrate lower overpotentials towards ORR.

### 1.3. Voltammetric Methods for ORR

For FCs, the main goal is to maximize the current since power output of a cell stack is directly related to current density. Electrochemical reactions are complex, and several processes affect current at the same time. To study these reactions, it is imperative to have controlled and standardized testing methods. Voltammetry among these methods is capable of probing information about reaction rate, kinetics and mass transfer on an

analyte. Voltammetry is essentially applying voltage to an electrode and recording the resulting current. The current is plotted against the potential and careful analysis reveal analytical information. In this thesis, a 3-electrode system is used to test catalytic activity in steady-state and in rotating disc electrode (RDE) setups. 3-electrode system employs working, reference and counter electrodes; the working electrode is where reaction of interest is examined, reference is used to control the applied potential to working electrode and counter electrode completes the circuit by passing most of the current flow through itself and not the reference.

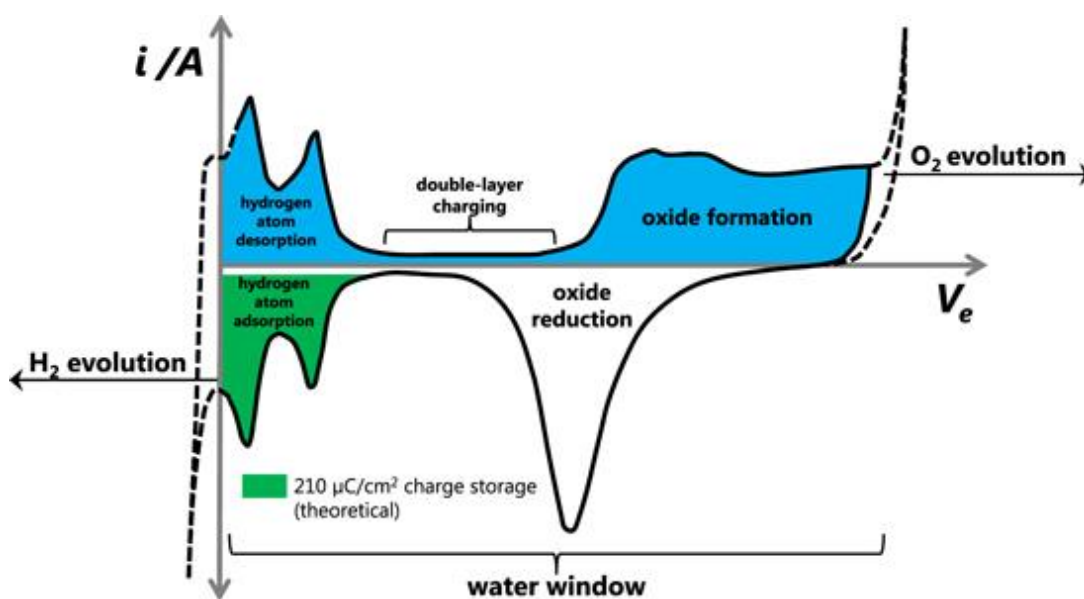


**Figure 5.** A textbook CV curve of Pt. Blue shaded area shows hydrogen desorption at low potential regime and Pt oxidation at higher potentials. Pt-O reduction is shown as unshaded area and hydrogen desorption is shown in green. Reprinted from Journal of Neural Engineering, Ref.<sup>10</sup>, under Creative Commons 3.0.

One of the most studied technique in a 3-electrode system is cyclic voltammetry (CV) which is of vital importance for electrocatalysts. In CV, working electrode is swept within a potential range back and forth to investigate adsorption-desorption and oxidation-reduction of the species of interest. Since mass transfer is limited, species undergo reactions during particular portions of the sweep and their concentration reduces, which terminates the reaction due to low reactant concentration. This gives a peak in the  $i$ - $V$  curve of CV and is easily interpretable for reversible operations. It is possible to recreate this behavior from the Butler-Volmer equation by modifying concentration term (making it zero for forward reaction) and overpotential term (making it underpotential for backwards reaction). For platinum-based electrodes, important regions in an  $i$ - $V$  curve are hydrogen desorption, platinum oxidation, platinum reduction and hydrogen

adsorption; these regions can be seen along with working window for aqueous solvents and hydrogen and oxygen evolution onsets in **Figure 5**. It is important to point out that this CV behavior is observed when the electrolyte has low oxygen concentration, otherwise the system would tend to perform ORR until mass transfer limits the current. Between the positive and negative sweep (or anodic and cathodic sweep) there is current contribution from a region called double layer capacitance which is not related to any faradaic process. It is possible to extract quantitative information from a CV scan of Pt based catalyst by integrating the hydrogen adsorption region, which falls between 0.075 to 0.4 vs reversible hydrogen electrode (RHE – a real reference electrode based on NHE) after subtraction of double layer capacitance<sup>11</sup>. This method relies on theoretical surface coverage of 1 cm<sup>2</sup> Pt with a monolayer of hydrogen, which requires about 210  $\mu\text{C}$  charge. By correcting for mass of Pt on electrode, one can obtain the electrochemical surface area of the catalyst, which will be elaborated in Experimental chapter.

It is possible to study ORR under hydrodynamic systems. RDE among them is widely adapted to literature because of its mode of mass transfer, which has been studied extensively and the simplicity of design. A rod of metal (e.g. Pt, Au) or other electrode material (e.g. glassy carbon) is covered with an insulating sheath and connected to the tip of a rotator. By controlling the rotation rate, it is possible to approximate the mass flux towards the electrode surface. To study ORR kinetics, linear sweep voltammetry (LSV) is used, where the potential is swept across a potential range only once and resulting shape of the currents are analyzed. Unlike CV, the electrolyte is purged with oxygen so that only oxygen reduction reaction is performed on the electrode under 1.23 V (standard potential of ORR). There is negligible contribution of hydrogen evolution reaction (HER) near 0.00 V which can be distinguished by the small decrease in current density. It is possible to directly retrieve information about overpotential, reaction onset and reversibility in an LSV experiment. Experimental LSV curves are given in **Figure 6**. In LSV for ORR, current is usually scanned from reducing potentials to oxidizing potentials (anodic sweep) and the result of the voltammogram can be explained in three parts;

- 1) Diffusion-limited region: this region corresponds to high ORR efficiency since overpotential is high. The current density in this region can be controlled by playing with mass transfer to the catalyst (rotation rate) since kinetics is fast and availability of oxygen determines the current density.

- 2) Kinetically-controlled region: this region corresponds to low overpotentials (or high applied potentials) thus the reaction is slow. Mass transfer does not contribute in this region as Pt is inactive at these potentials and activity depends solely on ORR kinetics.
- 3) Mixed region: in this region both mass transfer and kinetic current can contribute to the overall current density. It is imperative to analyze these region to obtain kinetic current, which is a measure of catalytic activity for the catalyst.

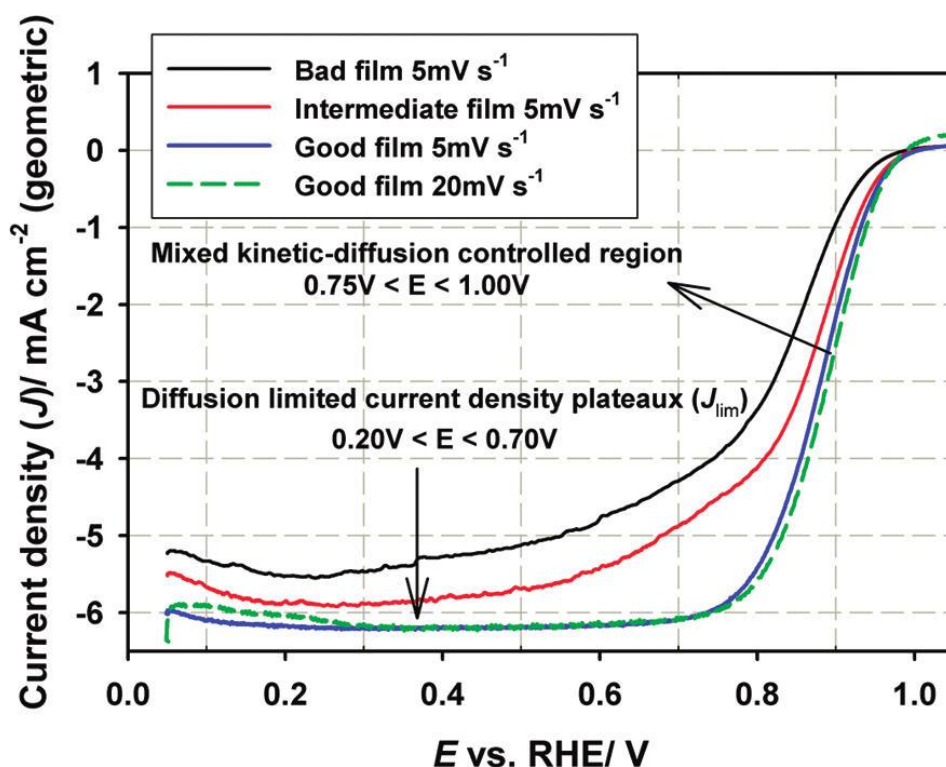


**Figure 6.** LSV curves for Pt/C catalysts in 3 different films and two scan rates in RDE test. Reprinted with permission from Analytical Chemistry, Ref<sup>11</sup>. Copyright 2010, American Chemical Society.

To elucidate mass transfer and kinetic contributions to current density, formulations by Koutecký and Levich are utilized. Levich modelled the mass transfer current (also called Levich current) as;

$$i_{l,c} = 0.62nFAD_0^{2/3}w^{1/2}\nu^{-1/6}C_0 \quad (1.15)$$

where  $n$  is the number of electrons transferred,  $w$  is the rotation rate (in radians per second),  $D$  is the diffusion coefficient of species 'O' and  $\nu$  is the kinematic viscosity. If one can obtain the limiting current from LSV scan (between 0.2 and 0.6 V), then by fitting

the current into Levich equation will yield important parameters based on the unknowns. One of the popular parameters to extract from Levich equation is number of electrons transferred. ORR is a 4-electron process so finding a number close to 4 may suggest minimal side reactions. Another important formula comes in the form of Koutecký-Levich equation, which enables finding the kinetic current from the mixed region of a voltammogram similar to **Figure 6**. Koutecký-Levich equation can be defined as;

$$\frac{1}{i} = \frac{1}{i_k} + \frac{1}{i_l} \quad OR \quad i = \frac{i_k i_l}{i_k + i_l} \quad (1.16)$$

where  $i_k$  is the so called kinetic current,  $i_l$  is the limiting current and  $i$  is the current measured at mixed region for ORR with moderate contribution from mass transfer, which is between limiting plateau and onset potential, and for Pt based catalysts taken at 0.8 to 0.9 V vs RHE. By obtaining kinetic current, researchers can find the actual activity of their catalyst free from mass transfer effects. The formula simulates what would happen if mass transfer were infinite to the electrode, which means reaction is only constrained kinetically. A demonstration of this effect can be seen when current is plotted against rotation rate for a slow kinetics process such as ORR in **Figure 7**.

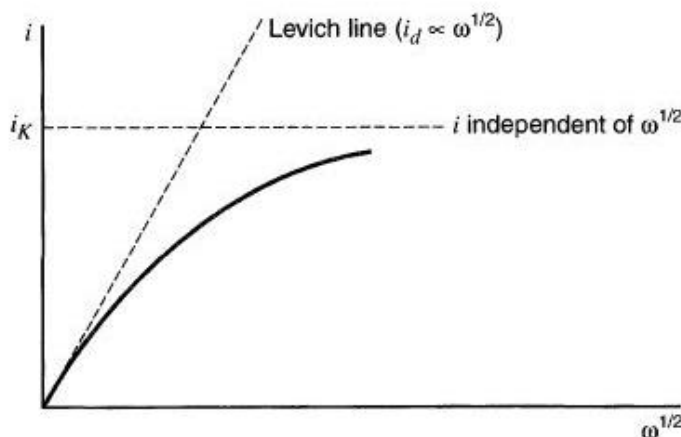


**Figure 7.** Deviation from ideal Levich line for a slow reaction. Reprinted with permission from John Wiley and Sons, *Electrochemical Methods: Fundamentals and Applications*, Ref<sup>5</sup>. Copyright 2001.

Upon this part the discussion revolved around ideal Pt catalysts. However, Pt is an expensive metal and not abundantly available. Since Pt has proven to be the highest activity catalyst in elemental form for acidic ORR, measures have been taken to maximize its surface area and decrease the cost. Next chapter will focus on support materials for Pt and other metals and even catalytically active supports.

## 1.4. Support Materials for ORR

Utilization of Pt (or other ORR active metals) depends on the support material that “anchors” these active metals on its surface. The support material should have a large surface area to hold as many active sites as possible, while having high porosity to facilitate transport of reactants and products<sup>12,13</sup>. It should hold active metals strongly environment of a fuel cell is essential as well<sup>13,14</sup>. Although it seems like finding a material that checks all these boxes impossible, numerous advancements in fuel cell and battery technologies has accelerated research in novel catalyst supports. Traditionally carbon has been used as catalyst support owing to its abundancy and established manufacturing techniques of several carbon materials such as activated carbon, carbon black and so on<sup>15</sup>. The idea behind using carbon as a support material arises from the need of an electrically conductive and relatively stable (in terms of pH and temperature) dispersant for active metal particles. It was later discovered that, supporting carbon structures in the case of Pt/C are not only an inert surface, but also an active constituent in catalysis due to its effects on the electronic properties of Pt<sup>16</sup>. With the explosion of interest in graphene and related materials, several interesting carbon-based structures have been developed and tested as support materials for ORR. In this chapter, some of the promising support materials will be introduced that are relevant to contemporary research trends and their advantages/disadvantages for ORR and fuel cell operation will be briefly discussed.

### 1.4.1. Carbon Black

Carbon black (CB) is an industrial carbon with turbostratic morphology and variable surface area (~50 to ~1500 cm<sup>2</sup>g<sup>-1</sup> BET surface area) produced by an incomplete burning of petroleum oils or acetylene<sup>17-19</sup>. The quality of starting materials makes it possible to have low ash content<sup>19</sup>, necessary for electrocatalytic processes. Since it is a relevant carbon for other industries as well, carbon blacks are cheap and abundant, making them attractive supports<sup>18</sup>. There is extensive literature on the use of CB as electrocatalyst supports due to mentioned properties, and research has revealed certain limitations of it; the impurities and carbon corrosion. Organo-sulfur impurities of carbon black adsorb quite strongly to Pt sites and prevent hydrogen splitting in the anode and oxygen splitting in the cathode<sup>20</sup>. This necessitates extensive cleaning of CB before any metal deposition reaction can take place. Carbon corrosion on the other hand is much more disastrous to the catalyst as it causes irreversible loss of Pt or Pt surface area by

dissolution and detachment mechanisms<sup>21</sup>. Strongly alkaline or acidic environments are corrosive for carbon blacks especially during high potential activities (like start-up/shutdown of a FC engine) and there is a need for kinetically stable carbon support<sup>22</sup>. These drawbacks of CB led researches to test other carbon materials as catalyst supports. A representative TEM image of commercial Pt/C catalyst (TKK) on Vulcan (Cabot Corp.) carbon can be seen in **Figure 8**.

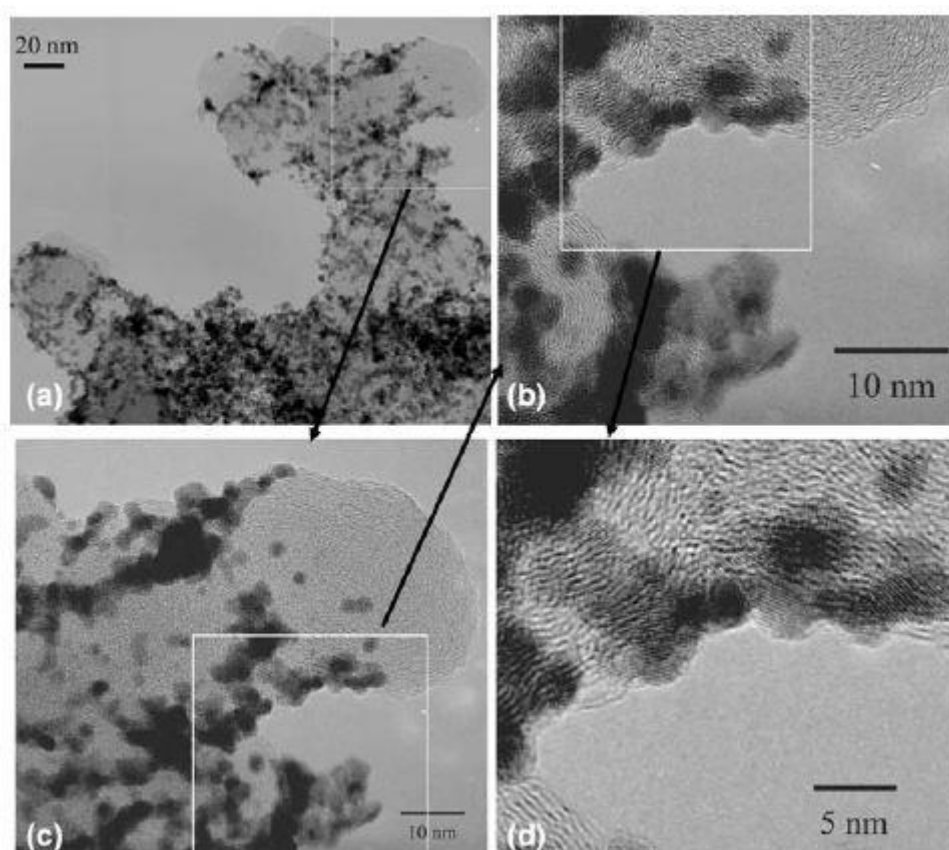


**Figure 8.** Pt NPs supported on carbon black (Vulcan) from low to high magnification (a, c, b to d). 2-3 nm sized Pt NPs are visible with poor dispersion on CB. Reprinted by permission from Springer Nature, Topics in Catalysis, Ref.<sup>21</sup>, Copyright 2007.

#### 1.4.2. Carbon Nanotubes

Carbon nanotubes (CNTs) are two dimensional hexagonally arranged carbons where ends of the graphitic plane rolls on itself on the edges. They have different possible structures in terms of number of layers; single-walled (SWCNTs) and multi-walled (MWCNTs) where single walled variety has a larger surface area and multi-walled ones are more conductive<sup>17</sup>. Both structure generally possesses larger surface area than carbon blacks and their highly crystalline structure makes them better electrical conductors. Research has shown increased activity in SWCNTs decorated with Pt nanodots compared

to Pt-Vulcan-XC72 (Pt/CB) for methanol electro-oxidation<sup>23</sup>. Stronger metal-support interaction and highly dispersed active sites are claimed to be responsible for the increased activity. MWCNTs are studied more extensively for electrocatalysis than their single-walled counterparts possibly due to higher durability and lower price. It was reported that MWCNTs sputtered with Pt nanodots have demonstrated superior performance in an FC system compared to Pt-CB type of catalysts<sup>24</sup>. Degradation of support structure and limited lifetime of catalyst layer are also important parameters for supports, and considering carbon black is plagued with corrosion problems, literature has revealed that significant increase in durability<sup>25</sup> and stability<sup>26</sup> can be achieved when MWCNTs are utilized. Effect of durability test on Pt-CB and Pt-MWCNT supports can be seen in **Figure 9**. Although there is some degree of aggregation in Pt-MWCNT, it is much more localized and to a lesser extent compared to Pt-Vulcan.

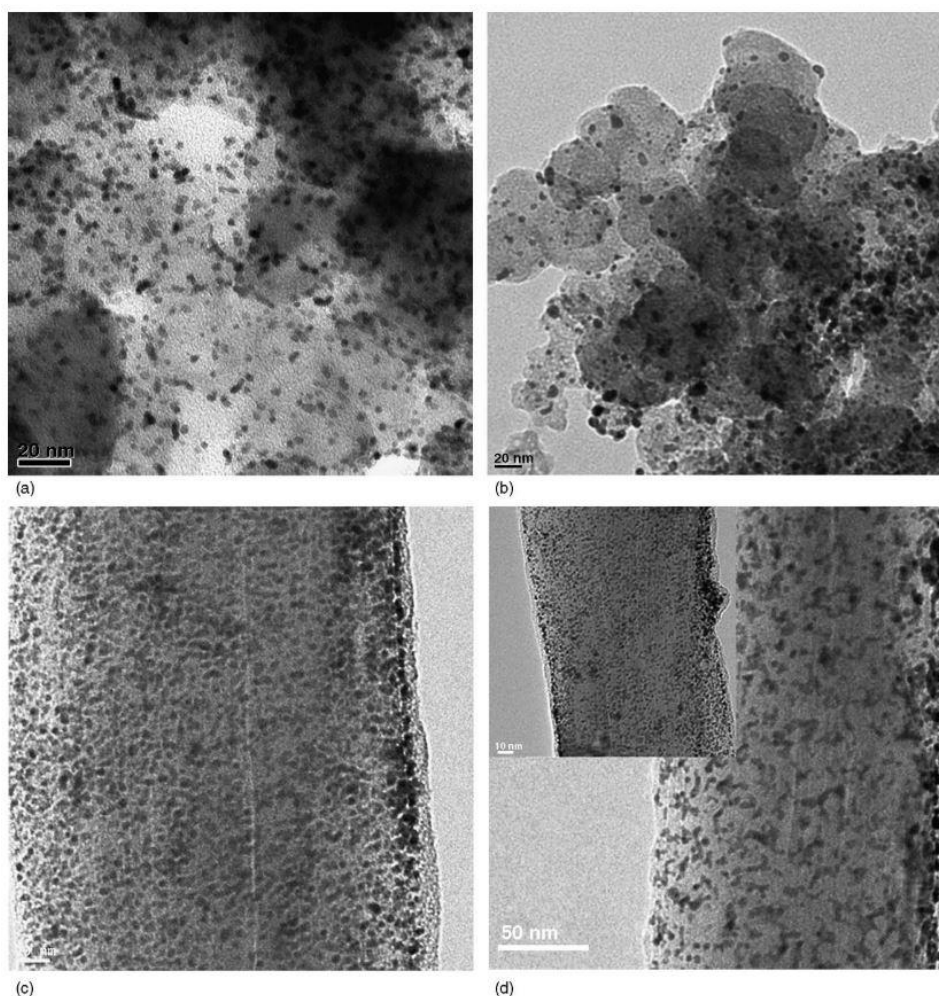


**Figure 9.** Pt-Vulcan before (a) and after (b) durability test. Pt-MWCNT before (c) and after (d) durability test. Reprinted with permission from Elsevier, Journal of Power Sources, Ref<sup>25</sup>, Copyright 2006.

However, there are several problems that need to be solved before CNTs become mainstream support material. Lack of intrinsic functional groups prohibit effective Pt deposition on these materials, which means an extra functionalization step must be applied to CNTs<sup>17</sup>. And although researchers are finding cheaper ways to produce CNTs<sup>27</sup>, it is still an expensive product (especially the single-walled variety), and that may increase already high FC stack costs.

### 1.4.3. Graphene & Graphene Oxide

Graphene is a remarkable material, discovered in 2004<sup>28</sup>, a single atom thick (2D) layer of carbon arranged in a hexagonal order. It can be considered as the building block of carbon nanotubes, fullerenes and graphite<sup>29</sup>. A representative image for different transformations of graphene can be seen in **Figure 10**. High conductivity coupled with extremely high theoretical surface area (near  $2600 \text{ m}^2\text{g}^{-1}$ )<sup>30</sup> made graphene an excellent candidate for support materials. However, single layer high quality graphene is difficult to produce in an industrial scale, so its usage may not be practical in a fuel cell system. It also suffers from lack of functional groups to anchor metal particles, similar to CNTs, though unlike CNTs graphene has an excellent precursor material in the form of graphene oxide (or graphite oxide depending on the level of exfoliation of individual sheets). Graphene oxide (GO) is made up of functionalized and stacked graphene layers that are separated from each other by covalently attached oxygen groups and adsorbed water molecules. Although it is not a decent conductor of electricity and has lower surface area than graphene, it is chemically tunable via its degree of oxidation and it can stabilize metal particles much more efficiently. Reduction of GO is also possible, which restores  $\pi$ -conjugation (and electrical conductivity) of the carbon and reduced graphene oxide (rGO), a defective and sparingly oxidized version of graphene, can be synthesized with such process<sup>31</sup>. It is also possible to simultaneously reduce metal salts and GO to achieve a conducting carbon support decorated with metal particles. Simultaneous reduction of metal salts and GO can achieve finely dispersed metal NPs on reduced graphene oxide with strong chemical interaction between graphene and the metal<sup>32</sup>.

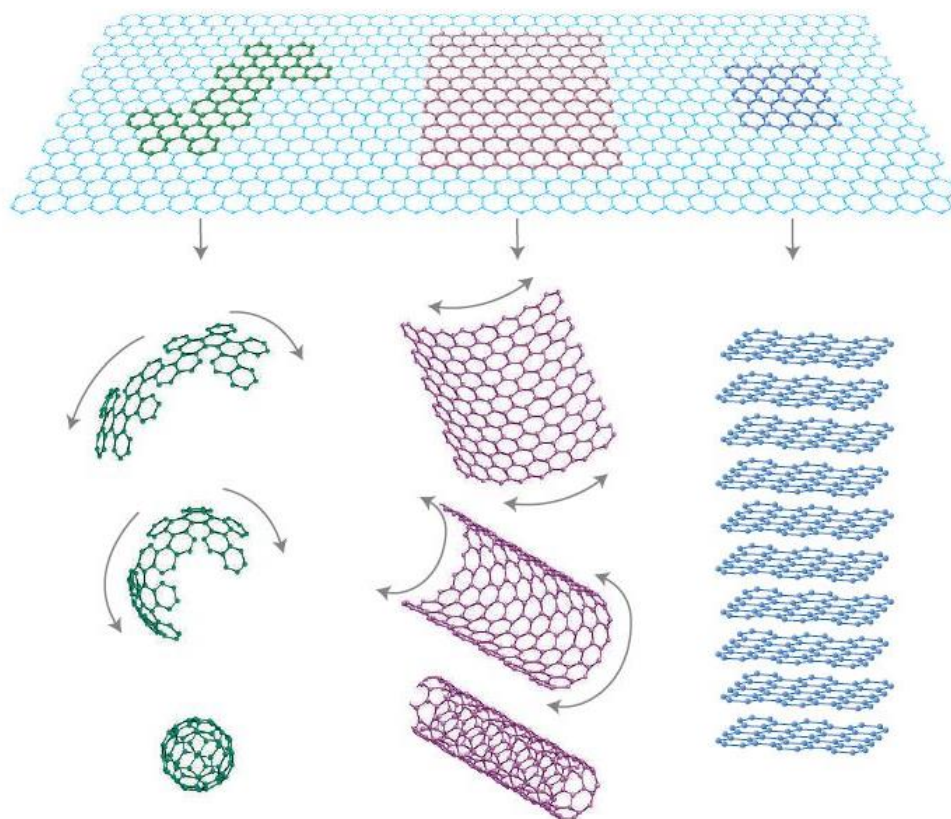


**Figure 10.** Wrapping graphene (2D) into fullerenes (0D) or rolling into carbon nanotubes (1D). Stacking layers of graphene makes graphite (3D). Reprinted with permission from Springer Nature, Nature Materials, Ref<sup>29</sup>, Copyright 2007.

Kou et. al has produced Pt decorated functionalized graphene sheets (FGSs) by thermal exfoliation and subsequent impregnation of Pt NPs. Their catalyst has demonstrated improved stability in an RDE setup compared to MWCNT analogue and commercial E-TEK (carbon cloth) catalyst, attributed to higher surface area and stabilizing surface groups of FGSs<sup>33</sup>. In a similar work, Shao et. al have observed improved durability for Pt nanoparticles deposited on graphene nanoplatelets (authors used this term for ~20 layers of stacked graphene with micro-sized lateral dimension) compared to E-TEK Pt/C and Pt/CNT catalyst<sup>34</sup>. Improved corrosion resistance and durability of Pt NPs deposited on graphene nanosheets compared to Pt/Vulcan XC-72 commercial catalyst has been shown by Wu et. al, where authors associated corrosion resistance with highly graphitic nature of graphene nanosheets<sup>35</sup>. Unfortunately, the improved durability and stability of graphene related structures are overshadowed by inconsistent ORR activity reports. There is a possibility that graphene layers hinder

oxygen diffusion in a FC catalyst due to its sheet like orientation<sup>36</sup>, which may reduce activity in mass transport controlled region of catalysts.

Given that the materials explained so far demonstrate excellent performance in particular requirements of an electrocatalyst support, researchers have tried to combine them to create so called hybrid structures.

#### 1.4.4. Hybrid Structures

Composite structures made from two carbon materials (such as rGO, CNT, CB, mesoporous carbon etc.) may inherit best qualities of both materials to reach improved durability and performance<sup>37</sup>. Catalysts incorporating hybrid supports of graphene-CNT<sup>38-41</sup>, CB-CNT<sup>42,43</sup> and graphene-CB<sup>44-46</sup> have been reported in literature and select examples among them is presented briefly below.

Sahoo et. al developed a rGO-MWCNT hybrid via catalysis-assisted chemical vapor deposition method (CCVD), decorated it with Pt and tested it against commercial Pt/C catalyst<sup>40</sup>. The authors reported increased performance in a PEMFC setup that is 71% higher than commercial catalyst. On a similar study, Yun et. al have synthesized Pt-graphene separately, mixed it with MWCNT and spray printed this mixture on a carbon cloth<sup>41</sup>. Authors have compared their novel catalyst against commercial Pt/CB and in-house Pt-graphene catalyst and found that Pt-graphene/MWCNT has performance between Pt/CB and Pt-graphene. The increased performance versus Pt-graphene is attributed to increased porosity and decreased charge transfer resistance induced by CNTs.

Some authors have decided to use carbon black as a spacer material for graphene (rGO) sheets. A representative image for catalyst scheme formed with graphene and spacer material can be found in **Figure 11**. Graphene sheets were decorated with Pt NPs and resulting material was simply mixed with CB in the study of Park et. al<sup>44</sup>. Authors have tested different concentrations of CB and found that 25% CB catalyst has higher electrochemical surface area and mass activity than bare Pt-G (Pt-graphene) catalyst. In the study by Li et. al, separately prepared Pt nanocrystals were deposited on rGO<sup>45</sup>. Resulting Pt-rGO were mixed with CB and tested against reference samples (Pt/CB) and intermediate samples of final catalyst (e.g. Pt-rGO). They have reported increased activity for the Pt/rGO/CB catalyst against Pt-rGO and increased durability against commercial

Pt/CB. It is predicted that rGO in this structure prevents Pt leaching into electrolyte by its sheet structure acting as a mesh and that dissolved Pt can nucleate on carbon black.

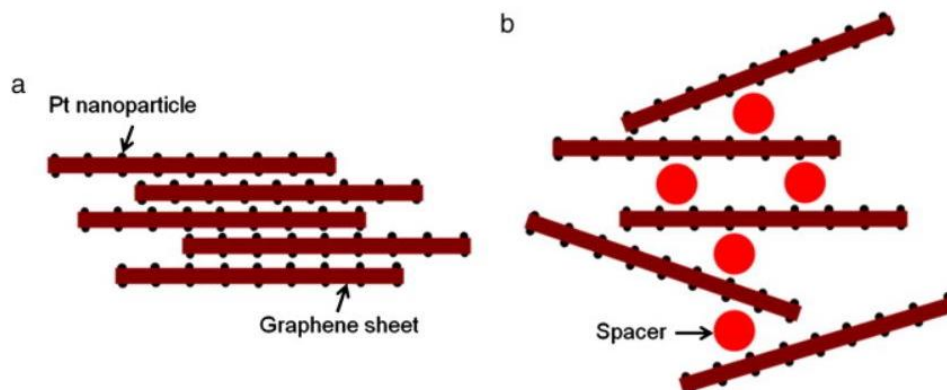


**Figure 11.** Catalyst layer with Pt on graphene (a) and Pt on graphene but with a spacer material in between (carbon black in the reference) (b). Reprinted with permission from Elsevier, *Electrochemistry Communications*, Ref<sup>44</sup>, Copyright 2011.

### 1.5. Metal-Organic Framework derived Supports & Catalysts

The search for excellent catalyst supports have impelled researchers to create novel carbon structures with improved mass transfer, decent metal anchoring capabilities and perhaps even innate catalytic activity towards ORR (usually facilitated by graphitic and pyridinic nitrogen atoms embedded in honeycomb lattice of carbon). A group of materials called metal-organic frameworks (MOFs) is anticipated to be exceptionally promising in that regard, especially for metal-free and non-PGM (platinum group metals) catalysts. This chapter will delve into the recent work on MOF derived carbonaceous structures both for PGM and non-PGM type of catalysts.

Metal-organic frameworks are coordination solids, where metal centers are connected to organic linkers to create a 3D crystalline structure<sup>47</sup>. MOFs have a well-defined structure and are “modifiable” by selection of metal clusters and organic linkers, also called as secondary building units. The linkers should have two or more functional sites for inorganic groups to bind and the properties of bonding (direction, bond strength etc.) determines the final structure of MOF. The effect of linker groups on network topology can be seen in **Figure 12**, where a class of MOFs made from same  $Zn_4O(CO_2)_6$  clusters but different organic linkers, called isorecticular MOFs (IRMOFs), are shown. Metal-organic framework structure can be pictured as strict symmetrical (octahedral, tetragonal etc.) metal clusters repeated by an organic unit in 3-D. The void spaces that are left between inorganic clusters form pores, that are connected to each other via narrower

“channels”, where pore size and channel diameter depends on the length of the organic chain. It is also vital that these pores and channels can be purged from the precursor solution or residual solvent molecules while maintaining structural integrity, so that foreign atoms can interact with pore and channel walls. High stability to temperature and chemical attacks, highly crystalline structure, high porosity (accessed by narrow channels) and modifiable nature of MOFs have made them attractive materials for applications ranging from separation of gases<sup>48</sup>, hydrogen storage<sup>49,50</sup>, gas adsorption<sup>51,52</sup>, battery<sup>53</sup> & fuel cell<sup>54–56</sup> systems and even for controlled drug delivery<sup>57</sup>.

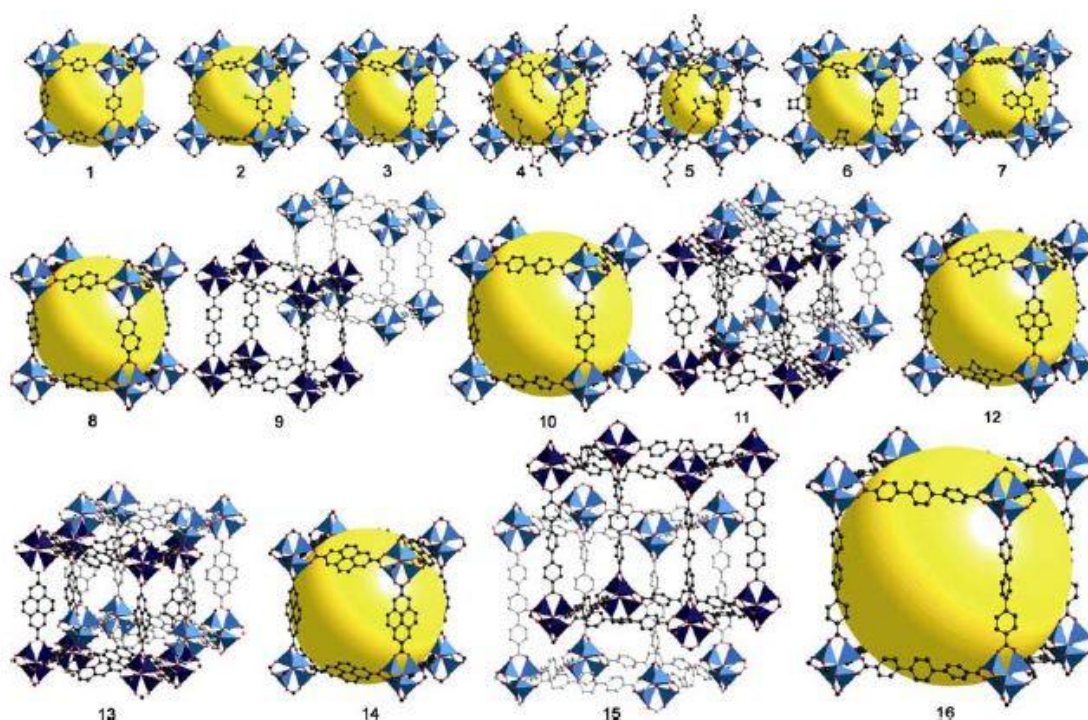


**Figure 12.** From 1 to 16, IRMOF structures with different organic linkers. Blue parts are basic zinc acetate clusters and yellow spheres represent void spaces within. Reprinted with permission from Elsevier, *Microporous and Mesoporous Materials*, Ref<sup>47</sup>, Copyright 2004.

MOFs can be used as a catalyst on their own, or as catalyst supports for PGM and non-PGM metals. The idea behind using MOFs as catalysts by themselves lie at the inherent catalytic activity of nitrogen-carbon moieties in alkaline media. Upon pyrolysis, a nitrogen containing MOF (e.g. imidazole as linker) transforms into nitrogen-carbon coordinated conductive structure if the metal is easily eliminated with acid leaching or in-situ removal. Such a case was demonstrated with in-situ synthesis of N-doped carbons from composites of zeolitic imidazolate framework-7 (ZIF-7) and glucose in the work of P. Zhang et. al<sup>58</sup>. The porosity of carbon (derived from ZIF-7 and glucose) increased the

number of and allowed easy access to active sites, and these active sites are hypothesized to be the result of the interaction between pyridinic nitrogen and  $\pi$ -network of carbon. Absence of elemental Zn in final catalyst is explained by an in-situ removal process aided by glucose. Final carbon structure in this work is active towards alkaline ORR. In a similar work by L. Zhang et. al, ZIF-8 derived carbon has been tested as an electrocatalyst in alkaline media<sup>59</sup>. Authors have used acid washing step to get rid of Zn impurities and reported that graphitic nitrogen (more than pyridinic nitrogen) is responsible for activity along with structural defects in carbon framework. The nature of activity in non-metal catalysts for ORR is still under debate as materials with different nitrogen moieties or even without nitrogen can perform relatively well in alkaline conditions.

Non-PGM catalysts are also promising for FC operation as PGM are expensive and are localized in a number of mines throughout the world<sup>60</sup>. Among non PGMs, Fe, Ni and Co are widely studied for ORR and there are MOF structures that can incorporate these metals and generate in-situ active sites upon pyrolysis. Zhao et. al have produced iron containing carbon nanoparticles from MIL-88B-NH<sub>2</sub> (Fe<sub>3</sub>O(NH<sub>2</sub>-BDC)<sub>3</sub>, NH<sub>2</sub>-BDC=2-aminoterephthalic acid) MOF by pyrolysis<sup>61</sup>. Resulting nitrogen containing carbon with iron coordination have improved ORR activity by 1.7-fold compared to Pt/C in Alkaline Direct Methanol Fuel Cell (ADMFC) system. The authors have attributed improved activity to presence of pyridinic nitrogen, Fe<sub>3</sub>C formation and high porosity. Cobalt is also one of the popular non-PGM catalysts and is part of an important MOF called ZIF-67 (Co(MeIM)<sub>2</sub>, MeIM=2-methylimidazole) which has been used in the study of Wang et. al as a sacrificial template to achieve Co-N<sub>x</sub> coordinated ORR active sites in carbon framework<sup>62</sup>. Resulting catalyst is active in alkaline and acidic environments and even surpasses activity of Pt/C in alkaline media. The active sites in this work is thought to be similar to Co-porphyrin coordination where cobalt atom is stabilized by nitrogen atoms in a macrocycle. A cobalt based active site generation proposed in a similar work has been demonstrated in **Figure 13**.

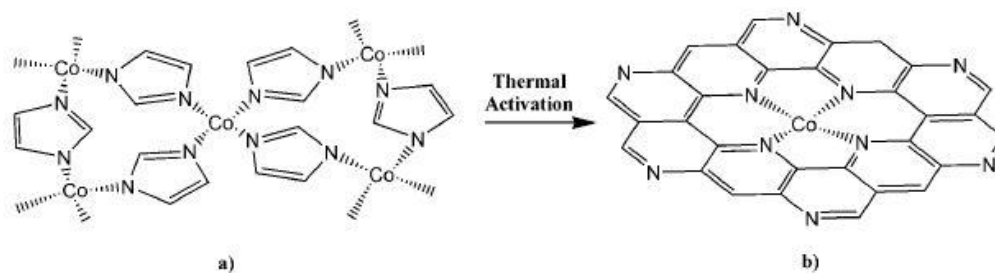


**Figure 13.** Proposed mechanism for active site generation in Co(Im)<sub>2</sub> MOF. Reprinted with permission from John Wiley and Sons, Chemistry – A European Journal, Ref<sup>63</sup>, Copyright 2011.

It is also possible to realize MOFs as simply support materials for extrinsic metals that are catalytically active. This approach allows researchers to be a bit freer on their MOF choice, since final carbon structure doesn't depend on the presence of in-situ generated metal sites. One of the most widely studied MOF is ZIF-8 which has zinc atoms tetrahedrally connected to 2-methylimidazole linkers through nitrogen atoms (ZnN<sub>4</sub> tetrahedra). It has high surface area owing to its microporous structure and has remarkable thermal and chemical stability, thus is promising for many catalytic applications<sup>64</sup>. In contrast with carboxylate linked MOFs, ZIF-8 has high nitrogen content which allows in-situ creation of nitrogen-doped carbon upon pyrolysis. Introduction of metal containing precursors to ZIF-8 prior to pyrolysis allows the metal atoms to coordinate with these carbon-nitrogen moieties and in both works cited below, catalytic activity is proposed to be dependent on Metal/Nitrogen/Carbon coordination environment, as first put forth by Jasinski in 1964<sup>65</sup>. In a groundbreaking study, Proietti et. al have mixed ZIF-8 with 1,10-phenanthroline and ferrous acetate, ball-milled, pyrolyzed in argon and then in ammonia to achieve an iron-based catalyst with highest volumetric activity of its time among non-PGM catalysts for ORR tested in a PEMFC setup<sup>56</sup>. Highly porous host combined with a carbon-nitrogen source (phenanthroline) and iron precursor seems to be a successful mixture for generation of non-PGM active sites. In a similar work Shui et. al have electrospun a mixture of ZIF-8, Tris-1,10-phenanthroline iron (II) perchlorate and electrospun this mixture in polyacrylonitrile-polymethylmethacrylate polymer blend<sup>66</sup>. This catalyst has microporous nanofibers hosting active sites separated by macropores (due to fibrous network) that allow efficient mass transport in a PEMFC setup. A schematic of this structure can be seen in **Figure 14**. In both cases, authors have tried to maximize iron, nitrogen and carbon amount in the catalyst by including iron containing (ferrous acetate or iron (II) perchlorate) and nitrogen containing (1,10-phenanthroline)

precursors and nitrogen containing MOF (ZIF-8) to create and nicely separate ORR active Fe/N/C groups. In the case of Shui et al., authors have also maximized mass transfer by designing a hierarchical structure composed of micropores and macropores.

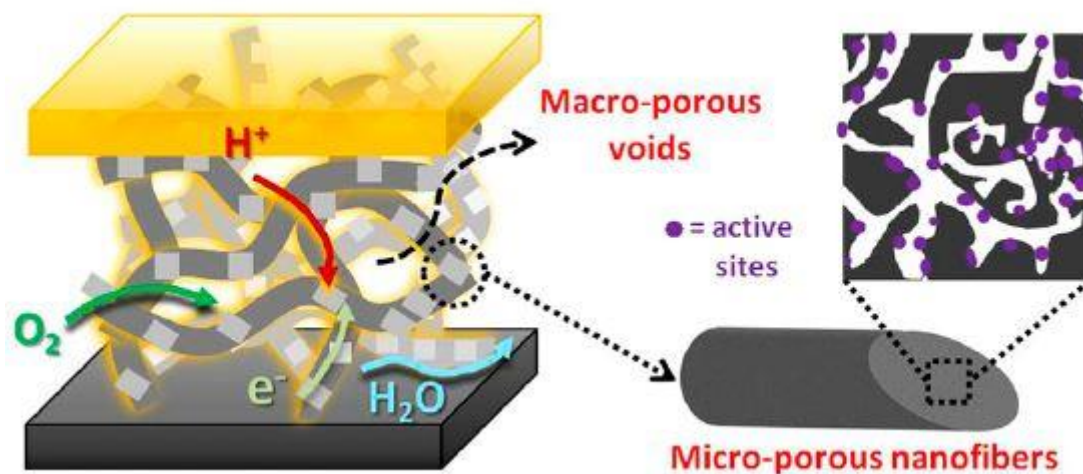


**Figure 14.** Macropores created by fiber network facilitate mass transport and micropores derived from ZIF-8 precursor host catalytically active sites. Reprinted from Shui et al.<sup>66</sup>, Proceedings of the National Academy of Sciences, 2015.

Obviously, a subset of the idea of supporting active metals with MOF based structures is supporting PGMs. These metals are proven to be efficient catalysts (Pt and Pd especially) for ORR so it is reasonable to combine MOF based supports with PGMs. A number of different approaches could be used to this end; for instance, Afsahi et. al have synthesized a Pt-based MOF by modifying an Al-based MOF called MOF-253<sup>67</sup>. The Pt atom in this framework is coordinated to the nitrogen atoms of bipyridine linker and is not actually part of the metal SBU. Following the synthesis, a pyrolysis step was applied to in-situ synthesize Pt NPs within the pyrolyzed MOF and Al metal was base leached before fuel cell tests. Although the method used in this study is promising, the catalyst has shown inferior activity at the cathode compared to commercial catalyst. Pt NP size in this study is also strongly affected by pyrolysis conditions. Nevertheless, the authors have suggested that using a reactive gas for pyrolysis may achieve better Pt dispersion in the MOF derived carbon. Instead of generating Pt NPs in situ, it is possible to synthesize the MOF around Pt NPs as done in the study of Qi et al<sup>68</sup>. The authors prepared Pt NPs, generated ZIF-8 around these NPs to achieve Pt@ ZIF-8 and then pyrolyzed Pt@ZIF-8. Rigid ZIF-8 structure prevented sintering of Pt NPs and Zn from ZIF-8 created intermetallic nanoparticles (iNPs) with Pt during pyrolysis. Authors have demonstrated smallest iNPs stable at 800 °C ( $2.4 \pm 0.4$  nm) and have shown that Pt-Zn

based catalyst has high tolerance to poisoning during MOR. It is also possible to deposit Pt NPs after the pyrolysis step of MOFs by conventional methods used for deposition on CB, graphene and CNTs. Khan et al. have pyrolyzed MOF-5 (also known as IRMOF-1, can be seen in Figure 5) and deposited Pt-Ni bimetallic NPs on top of this support by ethylene glycol reduction<sup>69</sup>. Their final catalyst Pt-Ni/PC 950 (15:15 wt% of Pt and Ni) has shown improved activity and durability compared to Pt/C (20%) in acidic media. This remarkable improvement is attributed to strong electronic interaction between Pt and Ni atoms and the underlying carbon support.

### **1.6. Summary & Motivation**

As seen from the previous examples of carbon (graphene, CB, CNT) and MOF-based supports, each structure has their merits with respect to ORR activity. CB is abundant and rigorously studied but has corrosion problems in a fuel cell system. Carbons such as graphene and CNTs have high durability in PEMFC setup and are highly conductive but may be too expensive to be practical as of yet. Comparatively new area of MOF-based carbons propose a promising approach to electrocatalyst and support design. These materials are 3-D structured, have high surface area and pores that facilitate catalyst dispersion and mass transfer. As hybrid systems impart their functionalities to final catalyst support and given that Pt and its alloys are still best performing catalysts in acidic conditions, a Pt incorporated MOF-based hybrid support could bring best of both worlds to the table.

GO is the first carbon structure that comes to mind for hybrid supports as it makes strong interaction with other materials through its surface functionalities. It is also possible to thermally reduce GO to rGO, which is more conductive and can be in-situ generated concurrently with the porous carbon (from pyrolysis of MOF). ZIF-8 is one of the most studied MOFs out there and synthesis methods have been improved to achieve rapid synthesis in room temperature and atmospheric pressure, in stark contrast with long synthesis times and temperatures for MOFs in general. Easily removable Zn sites is advantageous as well compared to other transition metal MOFs. However, most MOF-based hybrid approaches are either for non-PGM systems, focus on alkaline fuel cell environments or don't involve ORR process at all. There is a noticeable gap in literature when it comes to PGM deposited/incorporated MOF derived catalysts and their hybrid structures for ORR.

## 1.7. Aim & Objectives

The aim of this study is to synthesize an ORR catalyst based on platinum, ZIF-8 and graphene oxide. To this end, three main objectives can be surmised as;

- i) Synthesis of a ZIF-8/GO hybrid structure and thorough physical and chemical characterization of this hybrid at every step,
- ii) Subsequent pyrolysis and Pt decoration to reach a novel catalyst based on ZIF-8/GO,
- iii) Testing of this novel catalyst against reference materials with comparable structures to gain insight on the nature of ORR activity for this catalyst.

## 1.8. Novelty

It is the first time a MOF/GO hybrid has been used as a sacrificial carbon support for the deposition of Pt nanoparticles. There has been instances of ZIF-8/GO hybrids for ORR<sup>70,71</sup> but the authors have not studied acidic ORR activities or reported low activity. Pt in ZIF-8<sup>72,73</sup> and even Pt in ZIF-8/GO hybrids<sup>50</sup> are available in literature for variety of purposes, but not as ORR electrocatalysts. One study is inspiring in this sense; Qi et al. have demonstrated a way of ZIF-8 synthesis around Pt nanoparticles, but the study is limited in the sense that final nanoparticles have to be coordinated to zinc metal; they are intermetallic in nature<sup>68</sup>. It is imperative that Pt is integrated to ZIF-8 structure after pyrolysis to prevent such metal-metal coordination so that a controlled experiment only for the effect of support material can be constructed. Thus, a ZIF-8/GO hybrid derived porous carbon has been used as a support for Pt nanoparticles and tested for oxygen reduction reaction under acidic conditions.

## 2. EXPERIMENTAL

### 2.1. ZIF-8 and ZIF-8/GO Synthesis

Nanosized ZIF-8 were synthesized by excess ligand method that allows room temperature and aqueous synthesis conditions<sup>74</sup>. 1.17 g of zinc nitrate hexahydrate ( $\text{Zn}(\text{NO}_3)_2 \cdot 6\text{H}_2\text{O}$ , Sigma Aldrich) was dissolved in 8 mL of ultrapure water and were rapidly poured over a solution of 22.70 g of 2-methylimidazole (2-mIm, Sigma Aldrich) in 80 mL ultrapure water. The solution immediately turned into a white opaque color from transparent with a yellow tint, hinting that crystals have formed in seconds. The mixture is kept at room temperature for 5 minutes under vigorous stirring and then repeatedly centrifuged with DI water and ethanol. The final product was dried in a vacuum oven (VacuCell, MMM) for 24 hours under 60 °C.

ZIF-8/GO was synthesized during the synthetic procedure of MOF to ensure maximum interaction between ZIF-8 and GO. GO (GRAnPH) in 0.2571 g (100 wt% with respect to zinc metal amount) was added to the prepared 2-mIm solution. Exfoliation of GO was achieved by placing the mixture in an ice bath and sonicating with a probe sonicator (Q700, QSonica) for 1 hour. Rest of the procedure follows ZIF-8 synthesis parameters exactly. The yield is higher in the case of ZIF-8/GO, as GO flakes prevent MOF crystals from achieving stable colloids in water.

### 2.2. Pyrolysis of ZIF-8 and ZIF-8/GO

Pyrolysis is a necessary step for catalyst supports if the precursor materials are non-conductive like ZIF-8 or has low conductivity like ZIF-8/GO, as decent electrical contact between electrode-support (in this case, GCE-porous carbon) and support-catalyst (in this case, porous carbon-Pt NPs) and is vital to improve ORR activity. ZIF-8 and ZIF-8/GO were pyrolyzed in a sealed tube furnace at 650 °C for 2 hours. Positive pressure of Argon was constantly controlled by operator to prevent gas leaks into the tube. Also, furnace was purged with flowing Ar for 30 minutes before pyrolysis to reduce O<sub>2</sub> contamination. The temperature is selected to be just above the decomposition temperature of ZIF-8/GO, which is 600 °C as determined by TGA (can be seen in **Figure 15**). Resulting porous carbons are named as NC-0 (for pyrolyzed ZIF-8) and NC-1 (for pyrolyzed ZIF-8/GO).

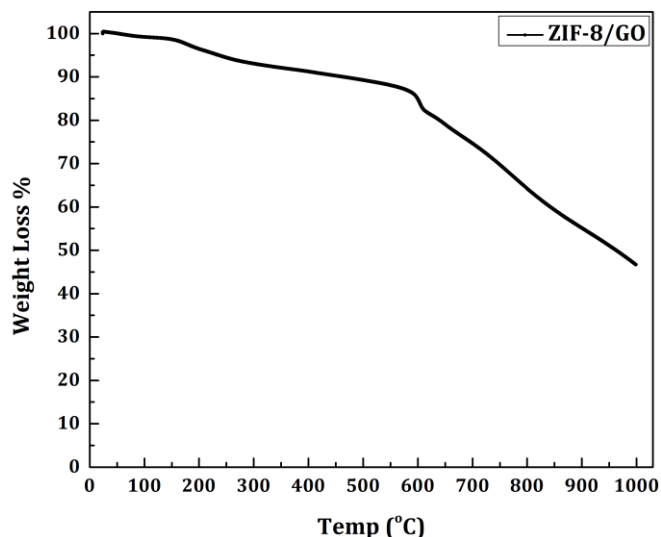


**Figure 15.** TGA of ZIF-8/GO in N<sub>2</sub> atmosphere.

### 2.3. Acid Wash of ZIF-8 and ZIF-8/GO

NC-0 and NC-1 were added to undiluted fuming hydrochloric acid (HCl, 37% w/w, Sigma Aldrich) and stirred for 1 hour. After acid washing, samples were washed with ample amount of DI water and dried in vacuum oven for 24 hours. These samples are also named as NC-0 and NC-1 as no characterization step was applied to non-washed samples. Throughout this thesis, all instances of NC-0 and NC-1 refers to acid washed varieties unless explicitly stated otherwise.

### 2.4. Pt Deposition on Porous Carbons via Polyol Method

NC-0 and NC-1 were decorated with Pt nanoparticles by a modification of polyol method<sup>75</sup>. 100 mg of porous carbon were dispersed in 120 mL of ethylene glycol (Sigma Aldrich), placed in an ice bath and sonicated for 1 hour in probe sonicator. 100 mg of Hexachloroplatinic acid hexahydrate (H<sub>2</sub>PtCl<sub>6</sub>.6H<sub>2</sub>O, 38% Pt basis, Sigma Aldrich) were dissolved in 5 mL of ultrapure water and mixed with sonicated ethylene glycol mixture. This mixture is transferred to a single neck glass flask and connected to a reflux line. The system is refluxed for 12 hours at 150 °C under mild stirring, left to cool in room temperature and repeatedly washed with ultrapure water. Catalysts were finally washed with reagent grade isopropyl alcohol (Sigma Aldrich) to prepare them for ink preparation step. Resultant solids were dried in vacuum oven at 60 °C for 24 hours and named as Cat-0 (for NC-0) and Cat-1 (for NC-1). To understand catalytic effects of ZIF-8, a reference sample was prepared. This time only pristine GO was dispersed in ethylene glycol and

rest of the procedure was kept same. This sample was named as Pt/r-GO due to reduction of GO in polyol method.

## 2.5. Characterization

X-ray Diffraction (XRD) were performed to reveal crystal structure of samples, between  $2\theta$  values of  $2-90^\circ$  with Bruker AXS D8 Advance diffractometer (Cu- $K\alpha$  line  $\lambda = 1.5406 \text{ \AA}$ ). To determine morphological structure of samples, a scanning electron microscope (Leo SUPRA 35VP FEG-SEM) was utilized at 5 kV accelerating voltage. Transmission Electron Microscope (TEM) was also employed to expand our understanding on distribution of Pt NPs and morphology of catalysts via Technai G2 F30 TEM in Bilkent UNAM (Bilkent University National Nanotechnology Research Center). Interplanar distances are calculated from fast Fourier Transformed (FFT) images of isolated NPs on catalysts via Digital Micrograph<sup>®</sup> software from Gatan Inc. Decomposition temperature of ZIF-8/GO was obtained with a Netzsch STA 449C thermogravimetric analyzer (TGA) under  $N_2$  atmosphere. Deposited Pt amount on samples were calculated based on the assumption that Pt would be the only species left after burning under air atmosphere, which was conducted in a Shimadzu DTG-60H TGA with 10 K heating rate from  $30^\circ\text{C}$  to  $1000^\circ\text{C}$ . The results were baseline corrected for detector drift, crucible impurities and residual ash content of GO, NC-0 and NC-1 to ensure accurate Pt amount determination. Fourier-transformed infrared spectroscopy (FT-IR) measurements were performed in a ThermoScientific Nicolet iS10 ATR FT-IR with a Ge-ATR detector.  $N_2$  isotherms were collected on a Micromeritics 3Flex Physisorption at 77.3 K temperature. All samples were degassed at  $160^\circ\text{C}$  for 24 hours before the sorption experiments.

## 2.6. Electrochemical Tests of Catalysts

Glassy carbon electrodes are polished to mirror finish prior to ink deposition by 3  $\mu\text{m}$  diamond suspension, followed by 1  $\mu\text{m}$  diamond suspension (Diapat-M, Metkon), bath sonication in ultrapure water for 5 minutes and drying with  $N_2$  flow. Catalyst inks were prepared considering the theoretical Pt distribution on GCE. The inks were formulated based on a water:IPA:Nafion<sup>®</sup> (20 wt%, Sigma Aldrich) ratio of 100:100:1, which is lower than most non-PGM catalyst inks but higher than suggested Pt/C catalyst inks, in terms of total Nafion<sup>®</sup> amount. It is suggested that lower amount is better for RDE setups since Nafion<sup>®</sup> complicates mass transport on electrode surface <sup>76</sup>.

For 20  $\mu\text{g}/\text{cm}^2$  Pt loading on 0.19625  $\text{cm}^2$  surface area, 3.925  $\mu\text{g}$  of Pt should be on electrode, which should originate from a single 10  $\mu\text{L}$  aliquot. The 38 wt% Pt basis precursor contributes at most 27.35 wt% Pt to the final catalyst for all samples, assuming all of the Pt ends up deposited on supports. Considering these, the final ink composition for Catalyst:Nafion<sup>®</sup>:Water:IPA ratio for all samples is as follows:

$$1.00 \text{ mg}:3.46 \mu\text{L}:346.66 \mu\text{L}:346.66 \mu\text{L} \quad (2.1)$$

Prepared inks were bath sonicated in ice filled water for 1 hour and immediately coated on a rotating disk electrode with a PTFE sheath and a surface area of 0.19625  $\text{cm}^2$  (Pine Instruments). Electrochemical tests were conducted in a 5-neck glass flask with Ag/AgCl as reference and Pt wire as counter electrode. Based on Nernst equation (1.4):

$$E_{\text{RHE}} = E_{\text{Ag}/\text{AgCl}} + 0.059\text{pH} + E^{\circ}_{\text{Ag}/\text{AgCl}}$$

$$E_{\text{RHE}} = E_{\text{Ag}/\text{AgCl}} + 0.059 + 0.1976 \text{ (for 0.1 M HClO}_4\text{)} \quad (2.2)$$

$$E_{\text{RHE}} = E_{\text{Ag}/\text{AgCl}} + 0.2566$$

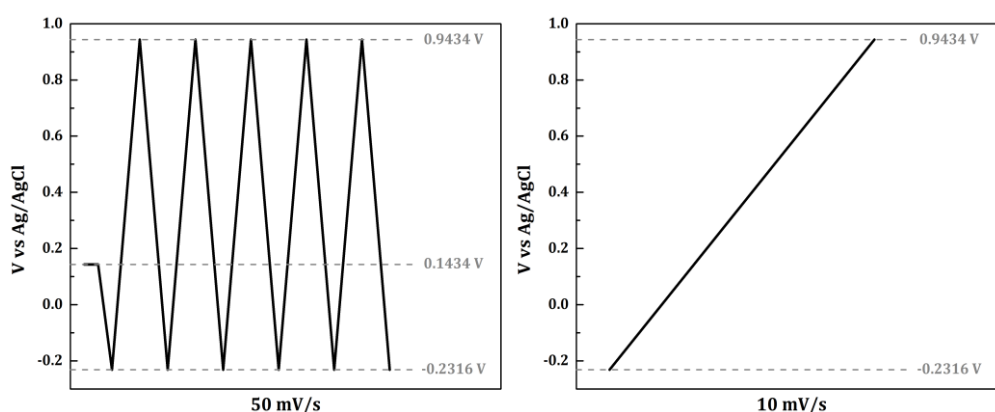


**Figure 16.** CV and LSV parameter correction for Ag/AgCl electrode

Thus, all potentials were corrected for Ag/AgCl electrode, which has 0.2566 V difference versus Reversible Hydrogen Electrode for our system (based on pH=1 for electrolyte and +0.1976 V of Ag/AgCl (in saturated KCl) standard potential at 25 °C). CV and LSV tests were conducted with a Gamry Reference 3000 potentiostat. For cyclic voltammetry (CV) tests, 0.1M HClO<sub>4</sub> (70% w/w, Sigma Aldrich) was employed as electrolyte since perchlorate ions has low adsorption on Pt. Electrolyte was purged with N<sub>2</sub> gas to reduce oxygen concentration. Electrodes covered with catalysts may have impurities and may require activation, so a 50-cycle conditioning step is conducted to prepare catalysts for electrochemical testing. Linear sweep voltammetry (LSV) tests require oxygen rich electrolyte to probe into ORR kinetics, so 0.1M HClO<sub>4</sub> were O<sub>2</sub>

purged. LSV tests were carried out at 1600 rpm to increase mass transport and conducted immediately after CV tests. Electrode surface is prohibited from contacting air between CV and LSV tests by a drop of electrolyte. Scan parameters corrected for Ag/AgCl electrode can be found in **Figure 16**.

### 3. RESULTS AND DISCUSSION

#### 3.1. GO as a Platform for ZIF-8 Growth

##### 3.1.1. Chemical perspective

Hybrid materials differ in terms of interaction between their constituents. A simple mixing approach may give a combination of constituent properties whereas a true hybrid structure may possess new properties arising from the interaction between species. The latter is present in the case of ZIF-8 and GO. By probing the chemical bonds of hybrid structure ZIF-8/GO, it is understood that MOF crystals are affected by the chemical environment GO creates in the precursor solution. In **Figure 17**, FT-IR analysis of ZIF-8, GO and ZIF-8/GO can be seen, whereas detailed peak designations of the materials are found in **Table 1**.

**Table 1.** FT-IR stretches of select functional groups in ZIF-8, GO and ZIF-8/GO.

Func. Group	Stretch
Carboxyl	1730 $\text{cm}^{-1}$
Hydroxyl	1230 $\text{cm}^{-1}$
Epoxide	1050 $\text{cm}^{-1}$
Imine	1590 $\text{cm}^{-1}$
Bound H <sub>2</sub> O	1600 $\text{cm}^{-1}$

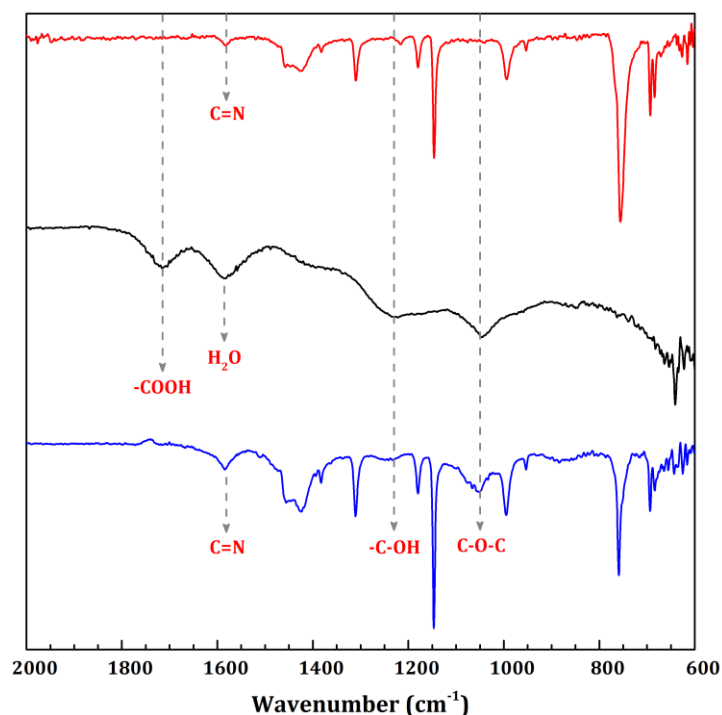


**Figure 17.** FT-IR graph of ZIF-8, GO and ZIF-8 GO from top to bottom can be seen. Important vibrations are affixed.

The fingerprint structure of ZIF-8 constitutes peaks mainly related to imidazole ring of linker group. One-to-one correspondence to ZIF-8/GO hybrid in terms of these peaks suggests that ZIF-8 chemical structure is not affected negatively by GO addition during synthesis. For GO on the other hand, peaks related to surface functionalities are visible, such as hydroxyl, carboxyl and epoxide stretches. Strong chemical interaction between ZIF-8 and GO is realized by an absence of these peaks in FT-IR graph of ZIF-8/GO hybrid. The underlying mechanism involves  $Zn^{+2}$  ions in synthesis conditions, coordinating to functional group sites and initiating the crystallization<sup>77</sup>. Epoxide group is not as affected as carboxyl and hydroxyl groups, suggesting lower interaction between epoxide and  $Zn^{+2}$  ions. Thus, with chemical interaction, it becomes possible to have a directed growth for ZIF-8 crystals on GO sheets.

### 3.1.2. Crystallographic perspective

Analogous to sodalite-type structure of natural zeolites, ZIF-8 crystals have zinc metal centers connected to 2-mIm linker units and form an infinite framework. GO however does not have a properly defined crystallinity; the degree of oxidation, which depends on synthesis conditions and efficiency, is directly correlated to interlayer spacing. However, it is still possible to get valuable information about GO in a diffractogram. In **Figure 18 (top)**, major reflections of GO and simulated peaks of graphite can be seen. The initial broad peak of GO near  $11.5^\circ$ , or  $7.68 \text{ \AA}$  as found by Bragg's law of diffraction, corresponds to (002) planes, that is reflection occurring between individual layers of graphene. Here a large FWHM indicates low crystallinity and that distance is not uniform between all layers. In graphite, this reflection occurs sharply at  $20.5^\circ$ , or  $4.32 \text{ \AA}$  separation, and can be seen from the simulated graph. As expected, GO has a larger interlayer distance due to its oxygen groups. In GO, there is also a peak near  $42.5^\circ$ , which could correspond to (100) or (101) in-plane reflections of graphitic layers. The broad hump between 20 and 30 degrees is from glass substrate holding the powder.

Crystallinity of ZIF-8 can give information about the success of synthesis, especially in the presence of GO. In **Figure 18 (bottom)**, major reflections of ZIF-8, ZIF-8/GO and simulated peaks of ZIF-8 are presented. First six reflections of zeolitic topology of ZIF-8 is also indexed in the graph. The near-perfect match of simulation with experimental peak positions is an indicator of successful ZIF-8 crystal formation. The strong reflection near  $38^\circ$  for ZIF-8 sample is caused by aluminum holder underneath. It

is not possible to see graphene oxide related reflections in ZIF-8/GO sample; the relative transparency of graphene to X-rays (compared to ZIF-8 crystals) and loss of order between graphene layers may be responsible for this behavior. Nevertheless, it is possible to determine presence of GO via other tools such as FT-IR and TEM.

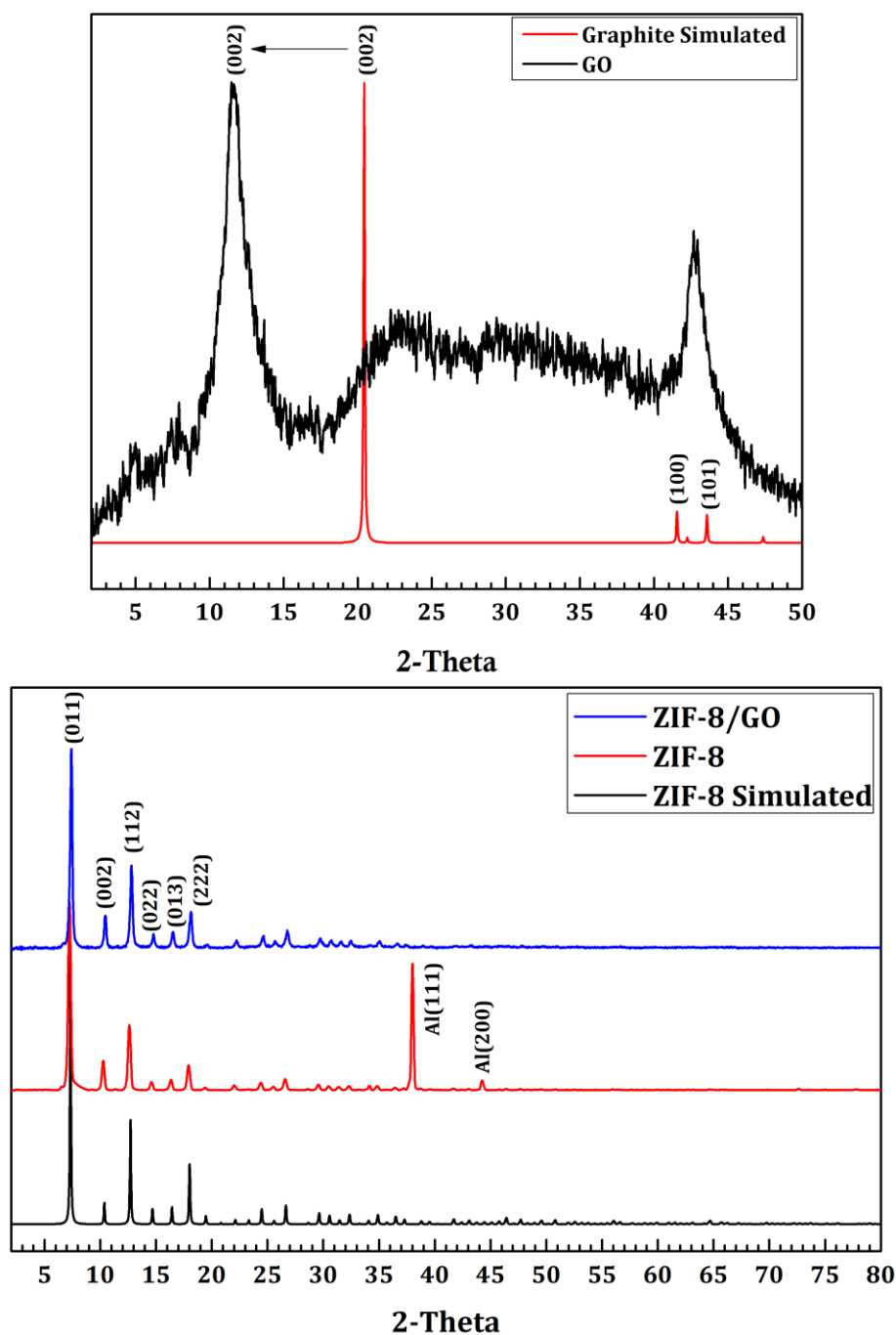


**Figure 18.** Simulated graphene and GO diffractograms (top) and simulated ZIF-8, as prepared ZIF-8 and hybrid ZIF-8/GO diffractograms (bottom).

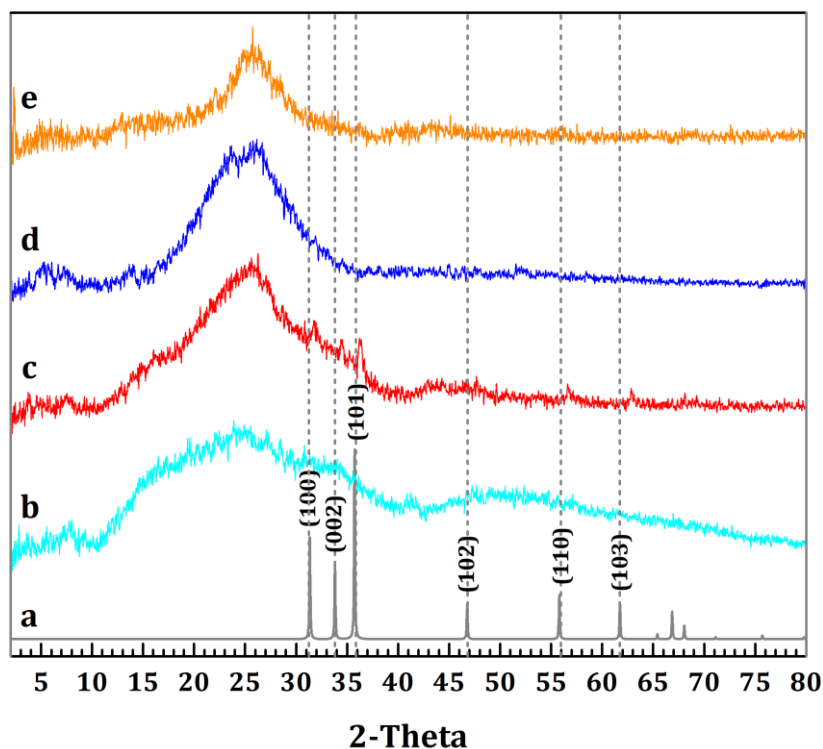


**Figure 19.** Simulated ZnO (a), non-washed NC-0 (b), non-washed NC-1 (c), acid washed NC-0 (d) and acid washed NC-1 (e).

MOF crystals are composed of metal centers that may be beneficial or detrimental to their performance depending on their usage scenario. In the case of ZIF-8 for electrocatalyst supports, the Zn centers may pose a problem, as they can only be partially removed from the support during the pyrolysis step (non-washed NC-0 of **Figure 19 (b)**). Zn centers of ZIF-8 oxidize into zinc oxide (ZnO) during heating, even in the low atmospheric oxygen concentration. Main culprit of such transformation is the washing step, which introduces solvents like ethanol and water, and these solvents can penetrate into ZIF-8 pores and even after vacuum treatment may stay there in residual amounts. Moreover, in the presence of oxygen functionalities of GO, this oxidation reaction is stronger as can be seen from the increased intensity of ZnO peaks for non-washed NC-1 (**Figure 19 (c)**). These oxide groups may leach during CV and LSV tests (due to highly acidic electrolyte) and may deteriorate the activity of the catalyst. Removal of ZnO peaks confirm the success of acid washing step since acid washed NC-0 (**Figure 19 (d)**) and NC-1 (**Figure 19 (e)**) doesn't have major ZnO reflections. The shift in ZnO peaks of non-washed NC-1 is caused by displacement error from powder sample preparation. On a final note, NC-0 and NC-1 has a single broad peak near 25 degrees, indicative of amorphous carbon.

### 3.1.3. Morphological perspective

The morphological evolution of samples from microporous crystals to porous carbons and finally to Pt containing catalysts can be seen in SEM pictures of **Figure 20**. Crystals may grow in a variety of shapes depending on the synthesis conditions and precursors. ZIF-8 crystals generated in this work have rhombic dodecahedron and spherical geometry, and they retain their structure even after pyrolysis and ethylene glycol reflux treatments, indicating that the framework is highly stable.

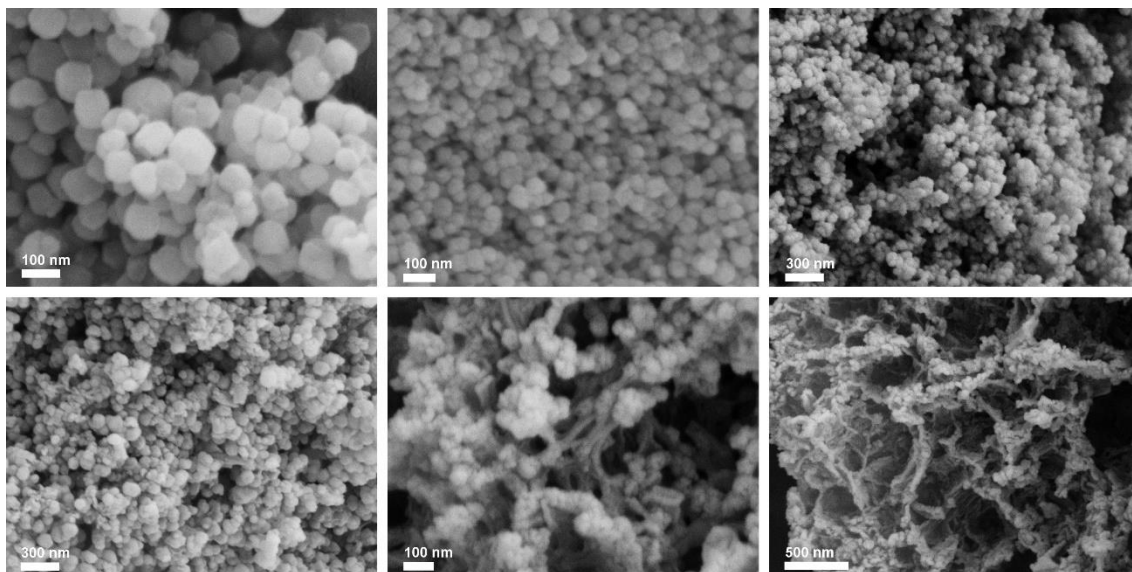


**Figure 20.** SEM micrographs of ZIF-8 (a), ZIF-8/GO (b), NC-0 (c), NC-1 (d), Cat-0 (e), Cat-1 (f).

Again, successful synthesis of ZIF-8 crystals in the presence of GO is confirmed, this time by the SEM pictures of ZIF-8/GO in **Figure 20 (b)**. The contrast between ZIF-8 and ZIF-8/GO derived porous carbons (**Figure 20 (c)** and **(d)** respectively) and catalysts (**Figure 20 (e)** and **(f)** respectively) is striking. NC-1 in **Figure 20 (d)** has a less aggregated structure and increased distance between individual ZIF-8 derived clusters, which is preserved in Cat-1 in **Figure 20 (f)** as well. The mechanism here could be depending on thermal reduction of GO and relaxation of hybrid structure, where ZIF-8 crystals are forced apart by the newly forming carbon mesh. Same cannot be said for the ZIF-8 derived porous carbon NC-0 in **Figure 20 (c)** and catalyst Cat-0 in **Figure 20 (e)**. Aggregation of crystals are visible in both images and morphology is kept intact throughout the pyrolysis and Pt deposition processes. It is not possible to see deposited Pt NPs in SEM images as they are much smaller than the resolvable distance by the equipment.

The SEM images give a more complete idea of morphology when considered with the results of sorption experiments.

### 3.1.4. Textural perspective

One of the established methods in the literature for porous material characterization is the nitrogen sorption experiments, and a widely used analysis is known as BET method for the multilayer adsorption theory proposed by Brunauer, Emmett and Teller in 1938<sup>78</sup>. Although BET method is not perfectly suitable for highly microporous materials such as ZIF-8, it gives a rough estimate on apparent surface area, and since it is extremely popular it is easy to compare findings with published results. The N<sub>2</sub> sorption isotherms of ZIF-8, ZIF-8/GO, NC-0 and NC-1 can be seen in **Figure 21**. Characteristic type-I isotherms, marked by a sharp increase at low relative pressures and flat response for rest of the adsorption process (except at the far end of the graph), are seen clearly on all samples, meaning ZIF-8 maintains its microporosity even after GO addition and pyrolysis. BET surface area of samples is calculated by:

$$S_{BET} = \frac{S_{cross-section}^{N_2} \times N_A \times V_m}{V_{molar}^{N_2}} \times \frac{1}{m} \quad (3.1)$$

where m is mass of adsorbent, N<sub>A</sub> is Avogadro's number, S<sub>cross-section</sub><sup>N<sub>2</sub></sup> is cross section and V<sub>molar</sub><sup>N<sub>2</sub></sup> is molar volume of N<sub>2</sub> molecule respectively. V<sub>m</sub> is calculated by:

$$V_m = \frac{1}{(I + A)} \quad (3.2)$$

where I is the intercept and A is the slope of a linear fit of;

$$BET_{(y-axis)} = \frac{1}{Volume\ Absorbed \times \left(\frac{1}{p/p_0} - 1\right)} \quad (3.3)$$

when it is plotted against relative pressure, p/p<sub>0</sub>. Nanosized ZIF-8 crystals have an apparent surface area of 1668 m<sup>2</sup>g<sup>-1</sup> in good agreement with literature, which reduces to 1152 m<sup>2</sup>g<sup>-1</sup> for ZIF-8/GO hybrid, due to low porosity of GO. Upon pyrolysis, these values further reduce to 685 m<sup>2</sup>g<sup>-1</sup> for NC-0 and 613 m<sup>2</sup>g<sup>-1</sup> for NC-1.

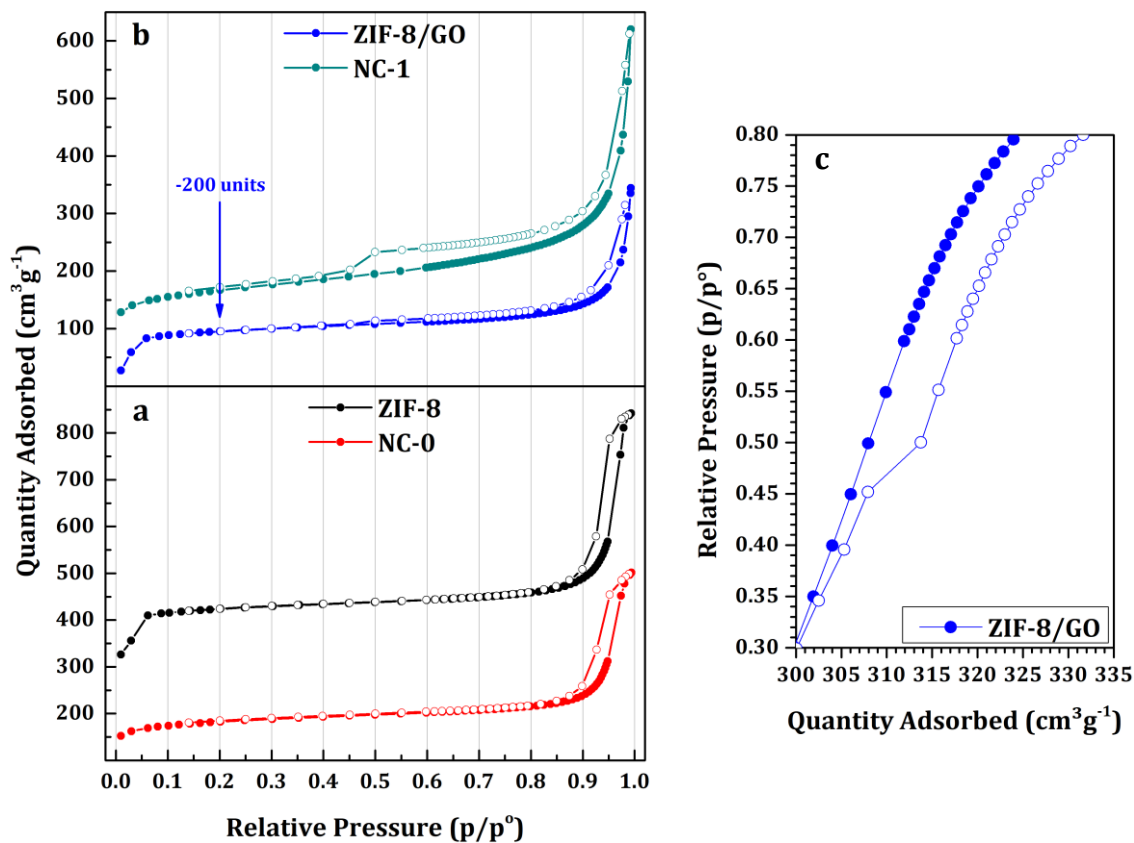


**Figure 21.** N<sub>2</sub> isotherms of ZIF-8 & NC-0 (a) and ZIF-8/GO & NC-1 (b). ZIF-8/GO is shifted -200 units to show hysteresis curves better. In (c) ZIF-8/GO is given with reversed axes to show intake behavior at mid-pressure range.

N<sub>2</sub> isotherms can also be categorized by their hysteresis behavior, where adsorption and desorption processes are not completely reversible. On the high relative pressures of ZIF-8 and NC-0 sample in **Figure 21** (a), an H1 type of hysteresis can be observed where the sharp increase is limited by a plateau. This hysteresis type is encountered when spherical particles leave empty spaces between them that are nearly uniform in size<sup>79,80</sup>, translating to aggregation and packing of nanosized ZIF-8 and (in the case of NC-0) ZIF-8 derived particles. Samples that have GO in them, ZIF-8/GO and NC-1, show composite hysteresis curves composed of H3 and H4 types in **Figure 21** (b) and enlarged graph in **Figure 21** (c). The H3 type has characteristic non-limiting increase in the adsorption curve at high relative pressures and has been seen in clay-like layered materials and/or slit-shaped pores<sup>79,80</sup>. The GO incorporation to ZIF-8 may have introduced such porosity and amplified it during pyrolysis since rGO is also a layered material. H4 type of hysteresis is observed in micro-mesoporous carbons and some mesoporous zeolites, distinguished from other types by an uptake at intermediate relative pressures, indicative

of micropore filling<sup>79,80</sup>. The intensity of both hysteresis curves increase from ZIF-8/GO to NC-1, suggesting that pyrolysis step is beneficial for hierarchical pore structure.

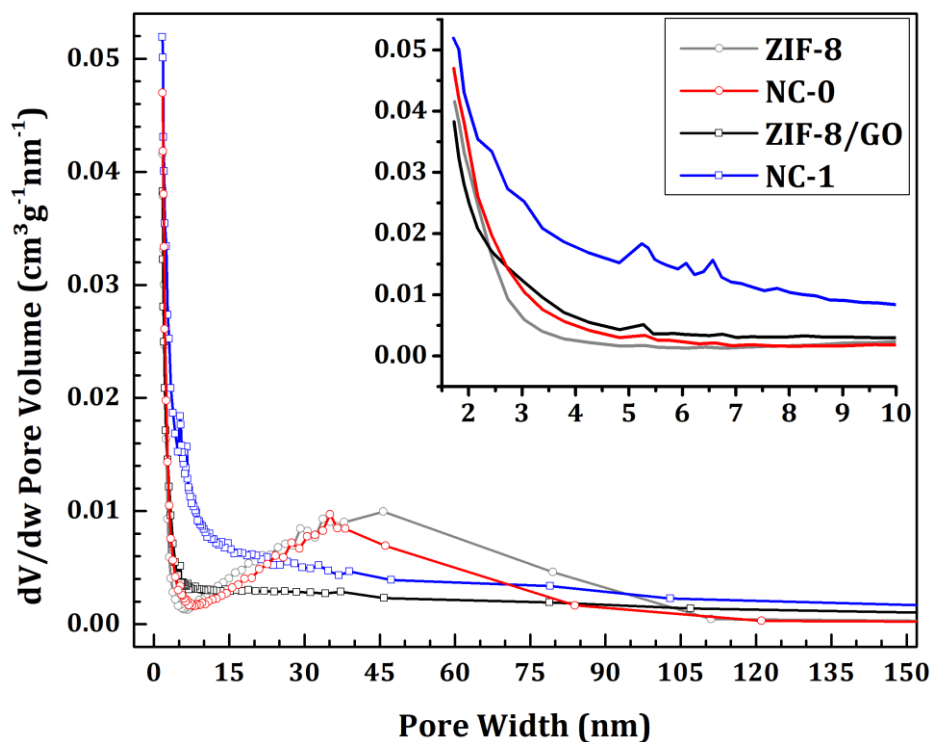


**Figure 22.** BJH pore size distribution of ZIF-8, ZIF-8/GO, NC-0 and NC-1. 2 to 10 nm range can be seen in the inset.

Pore size distribution is an important factor for mass transport properties of carbon-based supports. Smaller pores may facilitate catalytic activity by increasing the surface area and host active sites, whereas larger pores such as mesopores and macropores may improve flow of reactants and products of ORR reaction. Thus, Barrett-Joyner-Halenda (BJH) pore size analysis is performed on adsorption curves in **Figure 22**. The microporous range is not well resolved as expected since BJH analysis is more suited to deal with mesopores, but the graph suggest that there is a peak below 2 nm for all samples. ZIF-8 and NC-0 samples also demonstrate an average pore size in 30 to 50 nm range, in line with the previous explanation on uniform mesoporosity due to crystal packing and aggregation. Absence of this peak in ZIF-8/GO and NC-1 implies that GO has a scaffolding effect on ZIF-8 crystals by preventing their aggregative behavior. Meanwhile, GO can simultaneously introduce other sources of mesoporosity (from inset of **Figure 22**) and macroporosity as seen from higher  $dV/dw$  values of NC-1 compared to other samples for all pore width ranges. From **Table 2**, highest ratio of external to microporous surface area ( $S_{ext}/S_{micro}$ ) and pore volume ( $V_{total}$ ) of NC-1 sample also imply that

hierarchical porosity have been achieved by incorporation of GO to ZIF-8 and subsequent pyrolysis of the hybrid. Microporous surface area ( $S_{\text{micro}}$  – pores smaller than 2 nm) have been calculated by subtraction of external surface area ( $S_{\text{ext}}$  – pores larger than 2 nm) from total apparent surface area ( $S_{\text{total}}$ ) found by BET method. Ratio of external to microporous surface area is also reported for all samples as a reasonable measure of hierarchical porosity. Specific volume ( $V_{\text{total}}$ ) has been calculated from total adsorbate volume.

**Table 2.** Surface area calculation of ZIF-8, ZIF-8/GO, NC-0 and NC-1. All area units are in  $\text{m}^2\text{g}^{-1}$ .  $V_{\text{total}}$  is in  $\text{cm}^3\text{g}^{-1}$ .

	ZIF-8	ZIF-8/GO	NC-0	NC-1
$S_{\text{total}}$	1668	1152	685	613
$S_{\text{micro}}$	1547	1079	591	448
$S_{\text{ext}}$	93	72	94	165
$V_{\text{total}}$	0.70	0.43	0.55	0.79
$S_{\text{ext}}/S_{\text{micro}}$	0.06	0.066	0.16	0.36

### 3.2. Effect of ZIF-8 and GO on Electrochemical Performance

Performance of catalysts for ORR not only depends on the efficiency of deposited Pt NPs in catalysis and charge transfer, but also on efficiency of support materials to facilitate mass transport and conduction of electrons to close the circuit. Luckily, these aspects can be tested by powerful voltammetric methods (when supplementary characterization results are also taken into consideration) to reach a more or less complete picture of catalyst performance.

The deposition of Pt NPs is a physicochemical process where Pt groups adsorb on support surfaces by electrostatic forces facilitated by surface groups. To reveal successful deposition of Pt on supports, catalysts have been investigated in X-ray diffractometer, as seen in **Figure 23**. The calculated reflections of crystalline planes of Pt directly coincide with peaks of Cat-0, Cat-1 and Pt/rGO (which are broadened due to small crystal sizes of NPs), confirming presence of Pt on catalysts. The peak shift present in all samples compared to simulated graph is systematic and is probably caused by displacement error during powder sample preparation for measurement. The absence of such error in other graphs, e.g. **Figure 18**, arises from usage of different holders to accommodate for divergences in sample amount (pyrolysis and reflux have less than 100% yield).

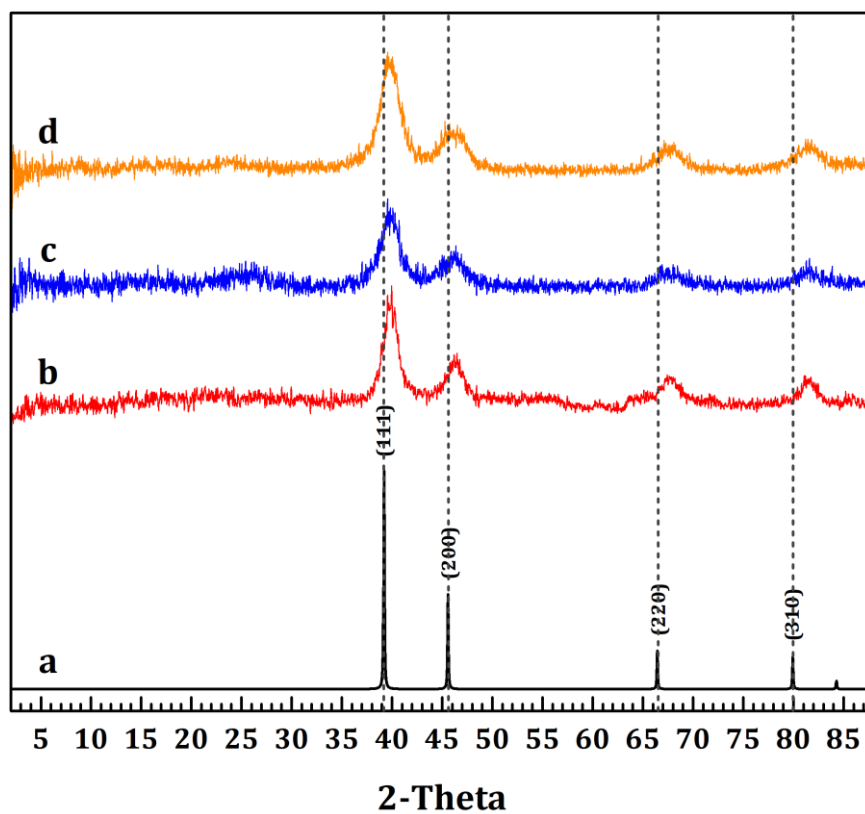


**Figure 23.** XRD graph of Simulated Pt (a), Cat-0 (b), Cat-1 (c) and Pt/rGO (d).

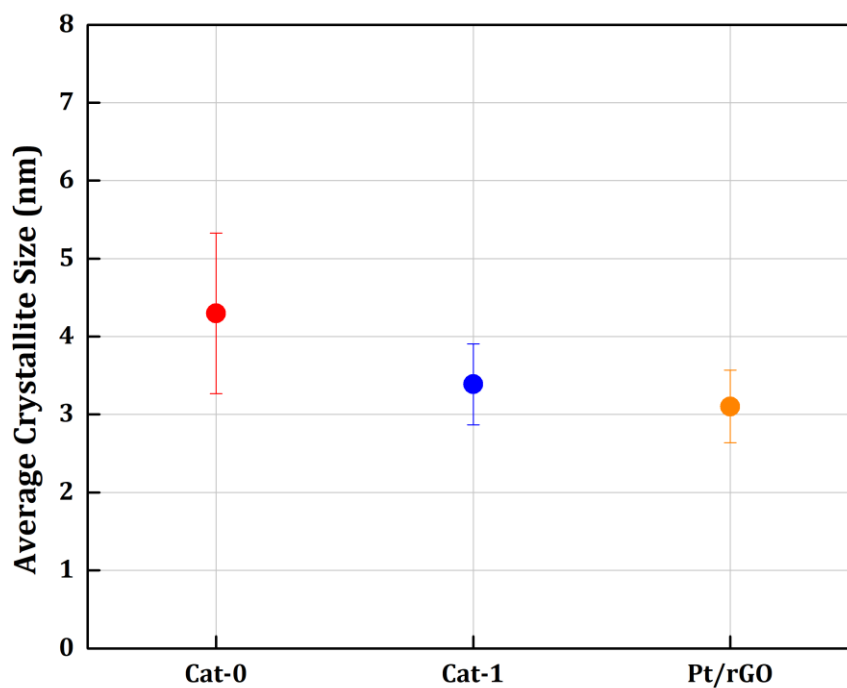


**Figure 24.** Average crystallite sizes of Cat-0, Cat-1 and Pt/rGO with error bars attached (n=4).

A useful information obtainable from diffractogram of nanoparticle-based materials is the crystallite size. Based on Scherrer equation, the crystallite size of catalysts can be calculated by:

$$\text{Crystallite size} = \frac{(K \times \lambda)}{FWHM \times \cos\theta} \quad (3.4)$$

where K is the structural constant (taken as 0.9 for the case of spherical NPs),  $\lambda$  is the wavelength of incident X-ray, FWHM is Full Width-Half Maximum of a gaussian fit of a reflection (the width of the peak in units of angle, taken at half the maximum intensity) and  $\theta$  is the position of this selected peak. For 3 samples analyzed, resolvable 4 most intense reflections of Pt [(111), (200), (220) and (310)] has been considered for crystallite size calculation. Based on this population, standard deviations have been calculated and given as error bars for each sample.

In the case of NPs, crystallite size coincides with particle size as most nanoparticles are single crystals and not polycrystalline. Average crystallite size decreases in order Cat-0 > Cat-1 > Pt/rGO (4.29 nm > 3.38 nm > 3.10 nm) and can be seen in **Figure 24**. Although the crystallite size difference is miniscule among samples, the reason behind it could be the amount of precursor GO (as crystallite size is inversely proportional to precursor GO amount). GO facilitates deposition of metal particles during chemical reduction<sup>32,81</sup> which results in lowest NP size in Pt/rGO. Since GO is thermally reduced to rGO after pyrolysis, NC-1 has lower concentration of functional groups than GO, which could be the reason behind larger Pt crystallite size of Cat-1. NC-0 does not have any graphene in it and the total absence of nucleation promoting graphene defects<sup>82</sup> in NC-0 may have caused lowest Pt crystallize size of Cat-0.

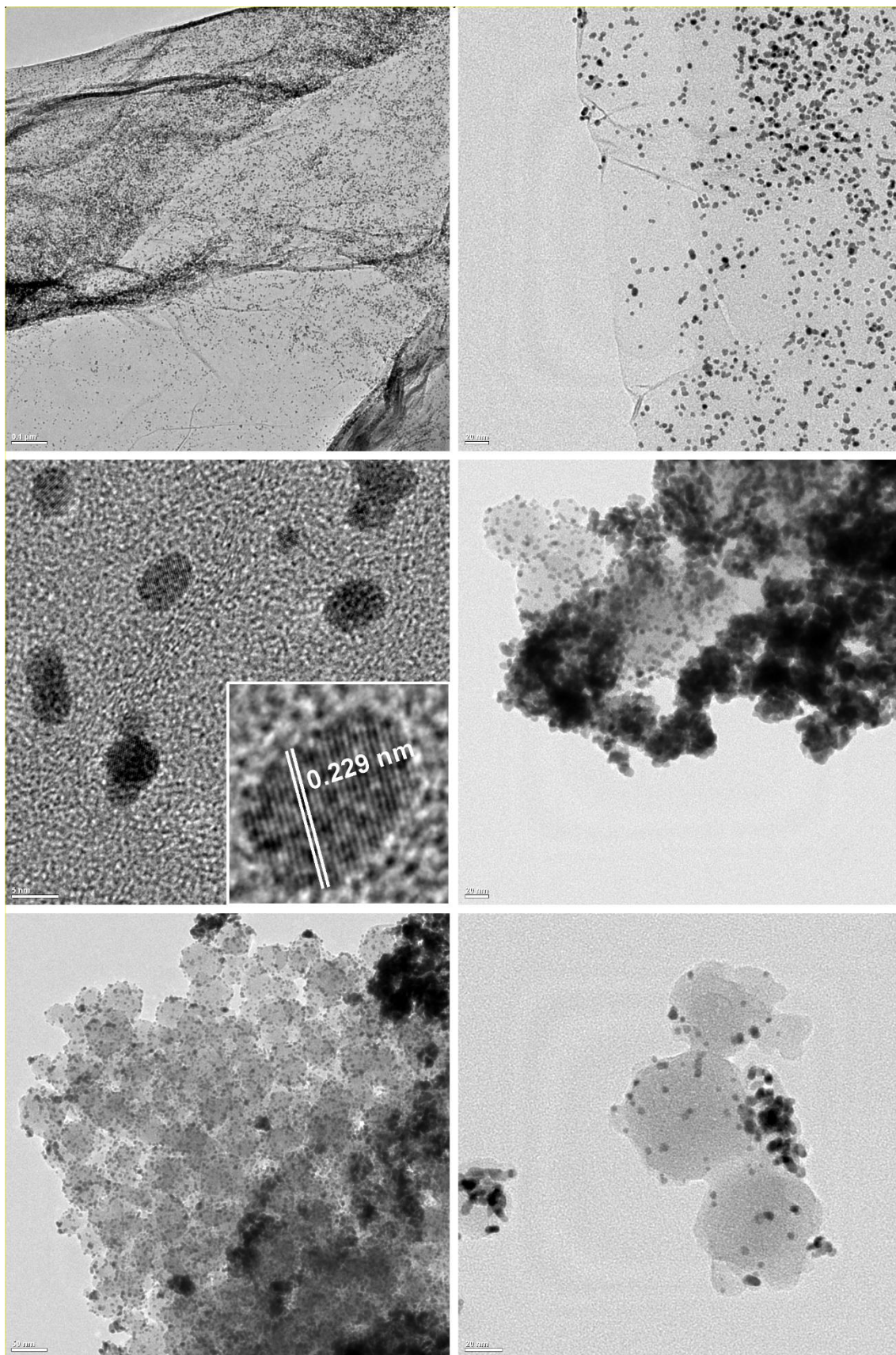


**Figure 25.** TEM images of Pt/rGO (a, b, c) and Cat-0 (d, e, f). Inset of (c) shows average interplanar spacing (111) of Pt NPs in Pt/rGO.

TEM images give a better picture on the dispersion of nanoparticles and final state of the catalyst. Pt NPs are finely dispersed with small particle size in Pt/rGO sample, as can be seen from **Figure 25 (a), (b) and (c)**. Flaky graphene structure and good separation of small particles are signature images for co-reduced Pt/rGO (Pt and GO reduced simultaneously) and have been encountered in literature previously<sup>75</sup>. Inset of **(c)** shows a single NP with average interplanar spacing of 0.229 nm, corresponding to separation distance of (111) planes of Pt<sup>83</sup>. Cat-0 sample can be seen in **Figure 25 (d), (e) and (f)** with its angular particles having a stark contrast with graphene. The porous carbon produced from ZIF-8 has kept its characteristic shape even after pyrolysis and EG reduction methods and did not undergo framework collapse. Pt NPs have a mixed dispersion on this support; most regions show good catalyst dispersion with small particle sizes in **(e) and (f)**, but some regions have aggregated particles as seen in black regions of **Figure 25 (d)**. Interestingly these regions are not composed of a single large nanoparticle, but many small particles aggregated in a specific shape. This shape is reminiscent of pyrolyzed ZIF-8 particles and suggests that Pt NPs have heavily nucleated inside the micropores of NC-0 during the reduction procedure. Previous observations for Pt@MOF structures determined that the method of impregnation is critical. Incipient wetness method produced aggregated Pt sites on MOFs through deposition on outer surface of crystals instead of its micropores<sup>68,84</sup>. Trying to introduce synthesized nanoparticles into synthesized MOF also proved to be futile as metal NPs are larger than cavities and channels of most MOFs. Building MOF crystals around already produced NPs created size controlled and finely dispersed active sites<sup>72</sup>, but in another study this method resulted in (and aimed for) intermetallic or alloy type structures after pyrolysis (PtZn, RuZn, etc.) since MOF precursors contain transition metals<sup>68</sup>. This approach is promising but not suitable for catalysts tested in this work where Pt is the only catalytically active metal and main investigation is the effect of MOF and GO on activity. By employing polyol-based reduction on pyrolyzed and acid washed MOF, Pt-Zn coordination is prevented, and controlled deposition of Pt NPs have been achieved with some degree of aggregation. Further investigation on the nature of these aggregated sites were conducted on Cat-1 sample by TEM-EDX analysis.

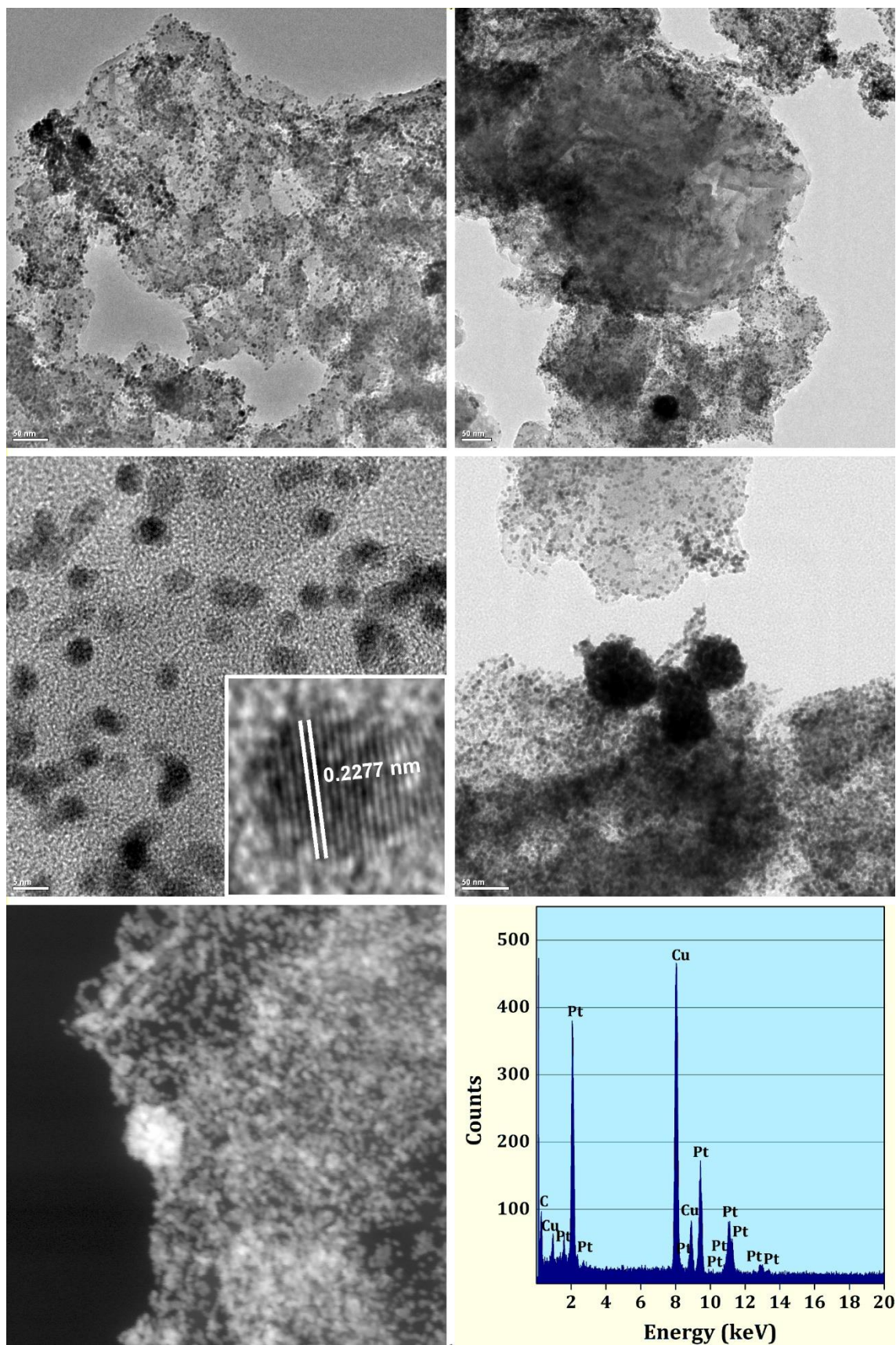


**Figure 26.** TEM images of Cat-1 (a), (b), (c) and (d). Inset of (c) shows average interplanar spacing (111) of a Pt NP on Cat-1. HAADF-STEM image of the unusual structure in Cat-1 (e) and its EDX analysis (f).

TEM images of Cat-1 sample can be found in **Figure 26 (a-e)**, demonstrating a hybrid structure of GO and pyrolyzed ZIF-8. Characteristic shape of ZIF-8 derived carbon is visible in **Figure 26 (a)** similar to the structures found in **Figure 26 (e)**, indicating that framework shape has been protected in this sample as well. Interesting sandwich structures can be seen throughout the sample (**a-b**), where ZIF-8 derived carbons are squeezed between graphene layers, and this morphology has been encountered in literature for pyrolyzed ZIF-8/GO composites previously<sup>70,71</sup>. Pt has good dispersion and forms small NPs on MOF derived carbon and GO derived graphene, and doesn't seem to favor one carbon type over the other in terms of deposition efficiency. The average interplanar distance for (111) planes are visible in the inset of (**c**) and is in acceptable agreement with previous findings. Unusual morphology encountered in Cat-0 is present here as well, albeit to a much lesser degree; some individual ZIF-8 derived porous carbons are full of Pt NPs that nucleated during reduction process and can be seen in one structure in (**b**) and four others in (**d**). To elucidate the nature of these clusters, a High-Angle Annular Dark Field image is taken in Scanning Transmission Electron Microscopy (HAADF-STEM) mode and can be seen in **Figure 26 (e)**. In this mode heavier elements are seen as brighter spots since more electrons can scatter from heavier nuclei with higher angles and fall on the annular detector. This time ZIF-8 derived carbon is brighter than neighboring structures which suggests presence of Pt inside it. Further analysis with Energy Dispersive X-ray (EDX) detector on that particular spot revealed the presence of Pt and C, with Cu signal arising from copper TEM grid as interference. Additional discussion on TEM images and the relation between activity (from electrochemical results) with dispersion and morphology (from TEM images) will take place further below in this chapter.

The amount of Pt that is deposited on catalyst supports is one of the most important parameters when catalysts of similar type are compared, since activity is usually reported in normalized units (per mass, per area etc.). To determine the amount of Pt, TG based mass analysis have been employed and its results are given in **Table 3**. The theoretical Pt wt% is calculated by assuming all Pt metal in precursor salt has deposited on carbon support and zero sample loss occurred during the reduction process. Exceptionally high Pt wt% of Pt/rGO is surprising but can be explained by removal of oxygen groups from GO in a reducing media. Respective sample loss from GO may have caused such a discrepancy between theoretical and TG based values.

**Table 3.** Theoretical and TG based Pt amounts and ECSA values of Cat-0, Cat-1 and Pt/rGO.

	Pt <sub>theoretical</sub> (wt%)	Pt <sub>actual</sub> (wt%)	ECSA (m <sup>2</sup> g <sub>Pt</sub> <sup>-1</sup> )
Cat-0	27	25	—
Cat-1	27	23	25
Pt/rGO	27	43	63

Cyclic voltammetry technique is widely employed in electrocatalyst characterization as it can simultaneously report kinetic and thermodynamic information about redox reactions. CV scans of Cat-0, Cat-1 and Pt/rGO in N<sub>2</sub> purged 0.1 M HClO<sub>4</sub> is given in **Figure 27**. Two important regions are visible in Pt/rGO and Cat-1; the hydrogen adsorption-desorption between 0.0-0.4 V, and Pt oxidation-reduction between 0.6-1.0 V. The H-adsorption charge (shown on **Figure 27** as hatched region) is particularly important for ORR catalysts as it indicates the electrochemically active surface area (EASA or ECSA), which is the area of Pt that has adsorbed hydrogen during the potential cycling. It is calculated by;

$$ECSA_{Pt}(m^2 g_{Pt}^{-1}) = \frac{Q_{H-adsorption} (Ccm^{-2})}{210\mu Ccm_{Pt}^{-2} \times L_{Pt}(mg_{Pt}cm^{-2})} \times 10^5 \quad (3.5)$$

where  $Q_{H-adsorption}$  is the charge found by integrating the respective region CV scans,  $210 \mu Ccm_{Pt}^{-2}$  is the conversion factor (fully covered polycrystalline Pt surface charge) and  $L_{Pt}$  is theoretical loading of Pt on working electrode surface (which is  $0.02 mgcm^{-2}$  on all samples). ECSA values of catalysts are given in **Table 3**.

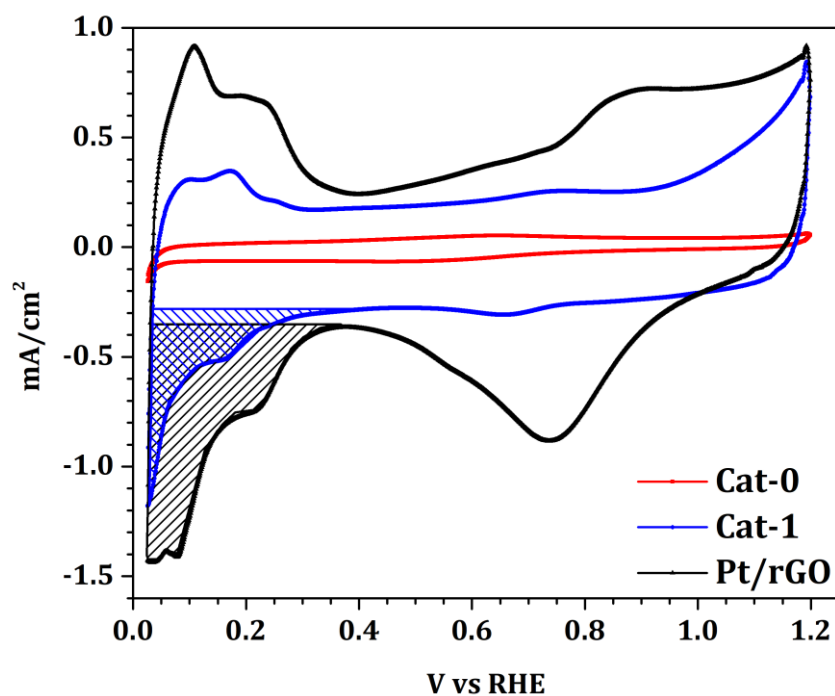


**Figure 27.** CV response of catalysts Cat-0, Cat-1 and Pt/rGO taken in  $N_2$  purged 0.1 M  $HClO_4$ . Hatched regions are hydrogen adsorption charges used for ECSA calculations.

Pt/rGO catalyst shows large and nicely defined H-adsorption region in CV graphs and consecutively has the highest ECSA value of  $62.90 \text{ m}^2_{\text{Pt}} \text{g}^{-1}$ . Nicely separated Pt sites with high accessibility to electrolyte in the immediate vicinity promotes hydrogen adsorption in Pt/rGO. Cat-1 has demonstrated lower ECSA than Pt/rGO, which could be related to lower amount of deposited Pt. It could also be attributed to trapped Pt NPs in the micropores of ZIF-8 derived carbon, which are not contributing to H-adsorption due to lack of contact with electrolyte. There have been instances as well on low hydrogen deposition efficiency in carbon encased metal NPs due to shielding effect of carbon around the active site<sup>68</sup>. CV scan of Cat-0 sample doesn't have any hydrogen-related regions and demonstrates capacitive behavior resulting from carbon support. Since TG analysis has proved that Pt is present in Cat-0, the logical explanation to such behavior is the aggregate structures observed in TEM images of Cat-0 in Figure 17. Similar to Cat-1, Cat-0 suffers from trapped Pt NPs lowering overall activity and this effect is much more dramatic here as Cat-0 seems to have higher amount of such structures. It is also likely that presence of rGO has improved overall conductivity<sup>71</sup>, and by extension ECSA, in Cat-1, which cannot be said for Cat-0.

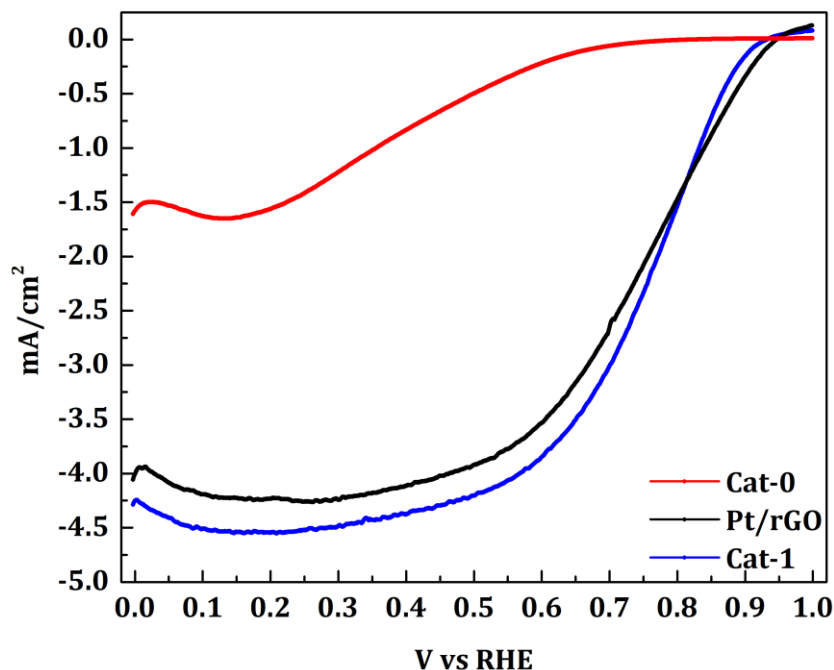


**Figure 28.** LSV scans in O<sub>2</sub> purged 0.1 M HClO<sub>4</sub> of Cat-0, Cat-1 and Pt/rGO.

Linear sweep voltammetry can be considered as a simpler version of CV, where a potential sweep in a specified direction is applied to the working electrode instead of cycling it and is usually employed where reactions with slow kinetics (quasi-reversible or irreversible reactions) are investigated. LSV scans of catalysts in O<sub>2</sub> purged 0.1 M HClO<sub>4</sub> are given in **Figure 28**. Again, Cat-0 sample doesn't demonstrate noteworthy activity, similar to its CV scan. The points discussed for its CV response is valid for its low ORR activity as well. In LSV scans, the diffusion-limited potential region of Cat-0 is not well resolved and does not form a plateau, which could mean this catalyst shifts to kinetically controlled ORR behavior quickly. This suggests Pt in Cat-0 has low access to oxygen in solution. The mass transfer is hindered not only because of trapped Pt sites but also due to aggregated structure of ZIF-8 derived carbon, best visible in SEM image of Cat-0 in **Figure 20 (e)**.

Cat-1 and Pt/rGO has similar polarization curves where Cat-1 has a slightly higher current density. Although the activity of Cat-1 and Pt/rGO looks quite similar in RDE polarization curves, they differ in magnitude when corrected for their Pt loading amount. From polarization curves one can obtain normalized currents that are measures of Pt mass-specific and "electrochemical area-specific" (also known as specific) activity. These currents are widely used in comparison of electrocatalysts in literature as they correct for variabilities in terms of catalyst loading and experimental variables. Mass

activity and specific activity can be calculated by kinetic current<sup>11</sup> (the current at the electrode if mass-transfer limitations did not exist) derived from the measured current by applying Koutecký-Levich equation of 1.16;

$$I_k = \left| \frac{I_d \times I}{I_d - I} \right| \quad (1.16)$$

Where  $I_k$  is the kinetic current,  $I_d$  is the diffusion-limited current measured at 0.4 V (vs RHE) and  $I$  is the measured current, at 0.8 V (vs RHE) for all catalysts in this thesis, obtained from voltammogram. The measured current should be in a potential where mass transport and diffusion act on catalysts at the same time, so called mixed kinetics region, and in Cat-1 and Pt/rGO this potential is taken at 0.8 V. From kinetic current ( $I_k$ ), a simple correction for mass of Pt on electrode surface reveals mass activity of Pt ( $I_m$ ) as:

$$I_m (A g^{-1}) = \frac{I_k}{Pt_{actual} (wt\%)} \quad (3.6)$$

where  $Pt_{actual}$  is the actual mass of Pt determined by mass spectroscopy or gravimetric methods, and in this work, it is determined by thermogravimetric analysis. Another normalized current, the specific activity of Pt ( $I_s$ ) is given by:

$$I_s (\mu A cm_{Pt}^{-2}) = \frac{I_k / A_g}{(Q_{H-adsorption} (C cm^{-2})) / (210 \mu C cm_{Pt}^{-2})} \quad (3.7)$$

where  $A_g$  is the surface area of working electrode (0.19625 cm<sup>2</sup>). Specific activity defines the current extracted from Pt per active area. A catalyst may give high ECSA but low current density which would reduce its specific activity. The mass and specific activity of Cat-1 and Pt/rGO can be found in **Figure 29**. Since it is not possible to extract meaningful kinetic current and ECSA data for Cat-0, its activity values are not calculated. The difference between Cat-1 and Pt/rGO is much more significant in mass and specific activity; Cat-1 has nearly double the mass activity and 2.5 times the specific activity of Pt/rGO. It is apparent that Pt is utilized much more efficiently in ZIF-8/GO derived catalyst.

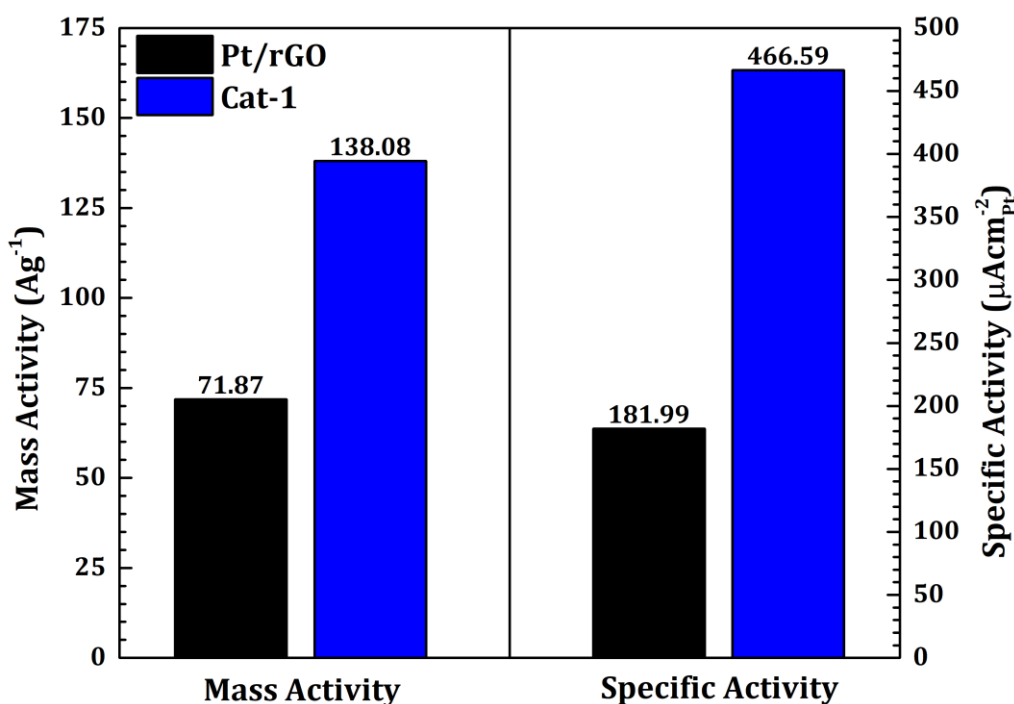


**Figure 29.** Mass activity and specific activity values of Cat-1 and Pt/rGO. Cat-0 is omitted due to missing ECSA and questionable kinetic current values.

When Cat-1 and Cat-0 is compared, we can see the effect of GO on performance of final catalyst. GO facilitates mass transport by preventing agglomeration of ZIF-8 derived carbon as revealed by SEM images and BET analysis of ZIF-8 derived (NC-0) and ZIF-8/GO derived (NC-1) carbons and TEM images of Cat-0 and Cat-1. Although ZIF-8 has the potential to host active sites efficiently, lack of larger pores and possibly lower conductivity after pyrolysis makes it an inferior catalyst support material. It is necessary to disperse and support this structure structurally and electrically with another material.

When Cat-1 and reference catalyst Pt/rGO is compared, we can see the effect of ZIF-8 as a precursor material for carbon supports. ZIF-8 derived carbon enables efficient mass transfer through its hierarchical porosity and framework structure, which in turn increases the utilization of Pt for ORR. Hindered mass transport in Pt/rGO possibly arise from stacking of rGO layers, which is prevented in Cat-1 due to 3-D structure of catalyst and exfoliating effect of ZIF-8 on graphene layers. The effect of ZIF-8 on mass transport is supported by concurrent investigation of CV and LSV graphs. The lackluster CV response, indicative of trapped Pt NPs, improves into superior ORR activity in case of Cat-1, meaning that reaction is accelerated by facile movement of ions to and from the Pt sites. This increase in transport properties of Cat-1 rectifies for the effects of micropore trapping and improves ORR kinetics of the catalyst.

#### 4. CONCLUSION

A novel catalyst based on Pt decorated ZIF-8/GO derived carbon (Cat-1) has been produced for the first time. Successful hybridization between ZIF-8 and GO has been revealed by analysis of FT-IR, XRD and nitrogen sorption experiments. Further examination of sorption experiments revealed that coordination of ZIF-8 and graphene oxide created hierarchical porosity upon pyrolysis, supported by SEM images. Successful deposition of Pt NPs were attributed to efficiency of EG reduction method; nanoparticle sizes are comparable with literature as revealed by TEM images and XRD diffractograms. Final catalyst structure resembles a sandwiched carbon, decorated with Pt nanoparticles as seen from TEM and SEM images. Cat-1 has been tested against reference materials of Pt/rGO and Pt decorated ZIF-8 derived carbon (Cat-0). Cat-1 has higher activity towards ORR than Pt/rGO and Cat-0. This effect is credited to hierarchical porosity and higher number of potential sites for Pt NPs. An interesting finding was that some Pt NPs have grown inside ZIF-8 derived carbons in excess amounts. This results in low ORR response for Cat-0 sample along with severely hindered mass transfer within ZIF-8 derived carbon aggregates. Although the trapped NP cluster morphology is more pronounced in Cat-0 sample, it is present to some degree in Cat-1 as well. This would reduce activity of Pt NPs that have limited/no contact with the electrolyte, which is supported by low ECSA values of Cat-1 and no ECSA response in Cat-0. Even though Cat-1 has lower ECSA, it has superior mass activity than Pt/rGO, which further signifies the substantial degree of mass transfer in this catalyst structure.

## BIBLIOGRAPHY

1. Edwards, P. P., Kuznetsov, V. L., David, W. I. F. & Brandon, N. P. Hydrogen and fuel cells: Towards a sustainable energy future. *Energy Policy* **36**, 4356–4362 (2008).
2. Clark, W. W. The green hydrogen paradigm shift: Energy generation for stations to vehicles. *Util. Policy* **16**, 117–129 (2008).
3. Barreto, L., Makihiro, A. & Riahi, K. The hydrogen economy in the 21st century: A sustainable development scenario. *Int. J. Hydrogen Energy* **28**, 267–284 (2003).
4. FuelCellToday - The leading authority on fuel cells. Available at: <http://www.fuelcelltoday.com/technologies/pemfc>.
5. Bard, A. J. & Faulkner, L. R. *Electrochemical methods: fundamentals and applications*. Wiley-Interscience (2001).
6. Nørskov, J. K. *et al.* Origin of the overpotential for oxygen reduction at a fuel-cell cathode. *J. Phys. Chem. B* **108**, 17886–17892 (2004).
7. Koper, M. T. M. Analysis of electrocatalytic reaction schemes: Distinction between rate-determining and potential-determining steps. *J. Solid State Electrochem.* **17**, 339–344 (2013).
8. Stamenkovic, V. R. *et al.* Improved Oxygen Reduction Activity on Pt<sub>3</sub>Ni(111) via Increased Surface Site Availability. *Science* (80-. ). **315**, 493–497 (2007).
9. Greeley, J. *et al.* Alloys of platinum and early transition metals as oxygen reduction electrocatalysts. *Nat. Chem.* **1**, 552–556 (2009).
10. Kumsa, D. W. *et al.* Electron transfer processes occurring on platinum neural stimulating electrodes: A tutorial on the i(Ve) profile. *J. Neural Eng.* **13**, (2016).
11. Garsany, Y., Baturina, O. A., Swider-Lyons, K. E. & Kocha, S. S. Experimental Methods for Quantifying the Activity of Platinum Electrocatalysts for the Oxygen Reduction Reaction. *Anal. Chem.* **82**, 6321–6328 (2010).
12. Li, Y., Fu, Z. Y. & Su, B. L. Hierarchically structured porous materials for energy conversion and storage. *Adv. Funct. Mater.* **22**, 4634–4667 (2012).
13. Antolini, E. Composite materials: An emerging class of fuel cell catalyst supports. *Appl. Catal. B Environ.* **100**, 413–426 (2010).
14. Gasteiger, H. A., Kocha, S. S., Sompalli, B. & Wagner, F. T. Activity benchmarks and requirements for Pt, Pt-alloy, and non-Pt oxygen reduction catalysts for PEMFCs. *Appl. Catal. B Environ.* **56**, 9–35 (2005).
15. Auer, E., Freund, A., Pietsch, J. & Tacke, T. Carbons as supports for industrial precious metal catalysts. *Appl. Catal. A Gen.* **173**, 259–271 (1998).
16. Yu, X. & Ye, S. Recent advances in activity and durability enhancement of Pt/C catalytic cathode in PEMFC. Part I. Physico-chemical and electronic interaction between Pt and carbon support, and activity enhancement of Pt/C catalyst. *J. Power Sources* **172**, 133–144 (2007).

17. Sharma, S. & Pollet, B. G. Support materials for PEMFC and DMFC electrocatalysts - A review. *J. Power Sources* **208**, 96–119 (2012).
18. Trogadas, P., Fuller, T. F. & Strasser, P. Carbon as catalyst and support for electrochemical energy conversion. *Carbon N. Y.* **75**, 5–42 (2014).
19. Antolini, E. Carbon supports for low-temperature fuel cell catalysts. *Appl. Catal. B Environ.* **88**, 1–24 (2009).
20. Garzon, F. H. *et al.* The impact of impurities on long term PEMFC performance. *ECS Trans.* **25**, 1575–1583 (2009).
21. Shao-Horn, Y. *et al.* Instability of supported platinum nanoparticles in low-temperature fuel cells. *Top. Catal.* **46**, 285–305 (2007).
22. Makharia, R. *et al.* Durable PEM Fuel Cell Electrode Materials: Requirements and Benchmarking Methodologies. *ECS Trans.* **1**, 3–18 (2006).
23. Wu, G., Chen, Y. S. & Xu, B. Q. Remarkable support effect of SWNTs in Pt catalyst for methanol electrooxidation. *Electrochem. commun.* **7**, 1237–1243 (2005).
24. Tang, Z. *et al.* Enhanced catalytic properties from platinum nanodots covered carbon nanotubes for proton-exchange membrane fuel cells. *J. Power Sources* **195**, 155–159 (2010).
25. Wang, X., Li, W., Chen, Z., Waje, M. & Yan, Y. Durability investigation of carbon nanotube as catalyst support for proton exchange membrane fuel cell. *J. Power Sources* **158**, 154–159 (2006).
26. Jiang, Z. Z. *et al.* Carbon-riveted Pt catalyst supported on nanocapsule MWCNTs-Al<sub>2</sub>O<sub>3</sub> with ultrahigh stability for high-temperature proton exchange membrane fuel cells. *Nanoscale* **4**, 7411–7418 (2012).
27. Mathur, R. B., Lal, C. & Sharma, D. K. Catalyst-free carbon nanotubes from coal-based material. *Energy Sources, Part A Recover. Util. Environ. Eff.* **29**, 21–27 (2007).
28. Novoselov, K. S. Electric Field Effect in Atomically Thin Carbon Films. *Science (80-. )*. **306**, 666–669 (2004).
29. A., G. & S., N. K. The rise of graphene. *Nat. Mater.* **6**, 183–191 (2007).
30. Peigney, A., Laurent, C., Flahaut, E., Bacsa, R. R. & Rousset, A. Specific surface area of carbon nanotubes and bundles of carbon nanotubes. *Carbon N. Y.* **39**, 507–514 (2001).
31. Dreyer, D. R., Park, S., Bielawski, C. W. & Ruoff, R. S. The chemistry of graphene oxide. *Chem. Soc. Rev.* **39**, 228–240 (2010).
32. Xue, Y. *et al.* Formation Mechanism and Cohesive Energy Analysis of Metal-Coated Graphene Nanocomposites Using In-Situ Co-Reduction Method. *Materials (Basel)*. **11**, 2071 (2018).
33. Kou, R. *et al.* Enhanced activity and stability of Pt catalysts on functionalized graphene sheets for electrocatalytic oxygen reduction. *Electrochem. commun.* **11**, 954–957 (2009).

34. Shao, Y. *et al.* Highly durable graphene nanoplatelets supported Pt nanocatalysts for oxygen reduction. *J. Power Sources* **195**, 4600–4605 (2010).
35. Wu, H., Wexler, D. & Liu, H. Durability investigation of graphene-supported Pt nanocatalysts for PEM fuel cells. *J. Solid State Electrochem.* **15**, 1057–1062 (2011).
36. Xin, Y. *et al.* Preparation and characterization of Pt supported on graphene with enhanced electrocatalytic activity in fuel cell. *J. Power Sources* **196**, 1012–1018 (2011).
37. Wang, Y. J., Fang, B., Li, H., Bi, X. T. & Wang, H. Progress in modified carbon support materials for Pt and Pt-alloy cathode catalysts in polymer electrolyte membrane fuel cells. *Prog. Mater. Sci.* **82**, 445–498 (2016).
38. Lv, R. *et al.* Open-ended, N-Doped carbon nanotube-graphene hybrid nanostructures as high-performance catalyst support. *Adv. Funct. Mater.* **21**, 999–1006 (2011).
39. Karthikeyan, N. *et al.* Highly durable platinum based cathode electrocatalysts for PEMFC application using oxygen and nitrogen functional groups attached nanocarbon supports. *Fuel Cells* **15**, 278–287 (2015).
40. Sahoo, M., Vinayan, B. P. & Ramaprabhu, S. Platinum-decorated chemically modified reduced graphene oxide-multiwalled carbon nanotube sandwich composite as cathode catalyst for a proton exchange membrane fuel cell. *RSC Adv.* **4**, 26140–26148 (2014).
41. Yun, Y. S., Kim, D., Tak, Y. & Jin, H. J. Porous graphene/carbon nanotube composite cathode for proton exchange membrane fuel cell. *Synth. Met.* **161**, 2460–2465 (2011).
42. NAKANO, H. *et al.* Carbon Nanotube and Carbon Black Supported Platinum Nanocomposites as Oxygen Reduction Electrocatalysts for Polymer Electrolyte Fuel Cells. *Electrochemistry* **75**, 705–708 (2007).
43. Xu, Y. & Li, X. Catalyst activity enhancement of PtRu/CB for methanol oxidation by carbon nanotube doping. *IEEE Trans. Nanotechnol.* **11**, 148–151 (2012).
44. Park, S. *et al.* Design of graphene sheets-supported Pt catalyst layer in PEM fuel cells. *Electrochem. commun.* **13**, 258–261 (2011).
45. Li, Y. *et al.* Stabilization of High-Performance Oxygen Reduction Reaction Pt Electrocatalyst Supported on Reduced Graphene Oxide/Carbon Black Composite. *J. Am. Chem. Soc.* **134**, 12326–12329 (2012).
46. Shervedani, R. K. & Amini, A. Carbon black/sulfur-doped graphene composite prepared by pyrolysis of graphene oxide with sodium polysulfide for oxygen reduction reaction. *Electrochim. Acta* **142**, 51–60 (2014).
47. Rowsell, J. L. C. & Yaghi, O. M. Metal-organic frameworks: A new class of porous materials. *Microporous Mesoporous Mater.* **73**, 3–14 (2004).
48. Chen, B., Xiang, S. & Qian, G. Metal-organic frameworks with functional pores for recognition of small molecules. *Acc. Chem. Res.* **43**, 1115–1124 (2010).

49. Proch, S. *et al.* Pt@MOF-177: Synthesis, room-temperature hydrogen storage and oxidation catalysis. *Chem. - A Eur. J.* **14**, 8204–8212 (2008).
50. Zhou, H. *et al.* High-capacity room-temperature hydrogen storage of zeolitic imidazolate framework/graphene oxide promoted by platinum metal catalyst. *Int. J. Hydrogen Energy* **40**, 12275–12285 (2015).
51. Kumari, G., Jayaramulu, K., Maji, T. K. & Narayana, C. Temperature induced structural transformations and gas adsorption in the zeolitic imidazolate framework ZIF-8: A Raman study. *J. Phys. Chem. A* **117**, 11006–11012 (2013).
52. Yaghi, O. M. *et al.* Control of Pore Size and Functionality in Isorecticular Zeolitic Imidazolate Frameworks and their Carbon Dioxide Selective Capture Properties. *J. Am. Chem. Soc.* **131**, 3875–+ (2009).
53. Zheng, F., Yang, Y. & Chen, Q. High lithium anodic performance of highly nitrogen-doped porous carbon prepared from a metal-organic framework. *Nat. Commun.* **5**, 5261 (2014).
54. Ren, Y., Chia, G. H. & Gao, Z. Metal-organic frameworks in fuel cell technologies. *Nano Today* **8**, 577–597 (2013).
55. Shui, J., Chen, C., Grabstanowicz, L., Zhao, D. & Liu, D.-J. Highly efficient nonprecious metal catalyst prepared with metal-organic framework in a continuous carbon nanofibrous network. *Proc. Natl. Acad. Sci.* **112**, 10629–10634 (2015).
56. Proietti, E. *et al.* Iron-based cathode catalyst with enhanced power density in polymer electrolyte membrane fuel cells. *Nat. Commun.* **2**, 1–6 (2011).
57. Horcajada, P. *et al.* Porous metal-organic-framework nanoscale carriers as a potential platform for drug delivery and imaging. *Nat. Mater.* **9**, 172–178 (2010).
58. Zhang, P. *et al.* ZIF-derived in situ nitrogen-doped porous carbons as efficient metal-free electrocatalysts for oxygen reduction reaction. *Energy Environ. Sci.* **7**, 442–450 (2014).
59. Zhang, L. *et al.* Highly graphitized nitrogen-doped porous carbon nanopolyhedra derived from ZIF-8 nanocrystals as efficient electrocatalysts for oxygen reduction reactions. *Nanoscale* **6**, 6590–6602 (2014).
60. Bloxham, L. *et al.* “Platinum 2013”. *Platin. Met. Rev.* **57**, 215–216 (2013).
61. Zhao, S. *et al.* Carbonized nanoscale metal-organic frameworks as high performance electrocatalyst for oxygen reduction reaction. *ACS Nano* **8**, 12660–12668 (2014).
62. Wang, X. *et al.* MOF derived catalysts for electrochemical oxygen reduction. *J. Mater. Chem. A* **2**, 14064–14070 (2014).
63. Ma, S., Goenaga, G. A., Call, A. V. & Liu, D. J. Cobalt imidazolate framework as precursor for oxygen reduction reaction electrocatalysts. *Chem. - A Eur. J.* **17**, 2063–2067 (2011).
64. Park, K. S. *et al.* Exceptional chemical and thermal stability of zeolitic imidazolate frameworks. *Proc. Natl. Acad. Sci.* **103**, 10186–10191 (2006).

65. Jasinski, R. A new fuel cell cathode catalyst [13]. *Nature* **201**, 1212–1213 (1964).
66. Shui, J., Chen, C., Grabstanowicz, L., Zhao, D. & Liu, D.-J. Highly efficient nonprecious metal catalyst prepared with metal–organic framework in a continuous carbon nanofibrous network - SI. *Proc. Natl. Acad. Sci.* **112**, 10629–10634 (2015).
67. Afsahi, F., Vinh-Thang, H., Mikhailenko, S. & Kaliaguine, S. Electrocatalyst synthesized from metal organic frameworks. *J. Power Sources* **239**, 415–423 (2013).
68. Qi, Z. *et al.* Conversion of confined metal@ZIF-8 structures to intermetallic nanoparticles supported on nitrogen-doped carbon for electrocatalysis. *Nano Res.* **11**, 3469–3479 (2018).
69. Khan, I. A., Qian, Y., Badshah, A., Nadeem, M. A. & Zhao, D. Highly Porous Carbon Derived from MOF-5 as a Support of ORR Electrocatalysts for Fuel Cells. *ACS Appl. Mater. Interfaces* **8**, 17268–17275 (2016).
70. Zhong, H. X. *et al.* ZIF-8 derived graphene-based nitrogen-doped porous carbon sheets as highly efficient and durable oxygen reduction electrocatalysts. *Angew. Chemie - Int. Ed.* **53**, 14235–14239 (2014).
71. Liu, S. *et al.* Metal-organic framework derived nitrogen-doped porous carbon@graphene sandwich-like structured composites as bifunctional electrocatalysts for oxygen reduction and evolution reactions. *Carbon N. Y.* **106**, 74–83 (2016).
72. Lu, G. *et al.* Imparting functionality to a metal-organic framework material by controlled nanoparticle encapsulation. *Nat. Chem.* **4**, 310–316 (2012).
73. Lee, S., Yim, C. & Jeon, S. Direct synthesis of platinum nanodots in ZIF-8/Fe<sub>3</sub>O<sub>4</sub> core–shell hybrid nanoparticles. *RSC Adv.* **7**, 31239–31243 (2017).
74. Pan, Y., Liu, Y., Zeng, G., Zhao, L. & Lai, Z. Rapid synthesis of zeolitic imidazolate framework-8 (ZIF-8) nanocrystals in an aqueous system. *Chem. Commun.* **47**, 2071–2073 (2011).
75. Şanlı, L. I., Bayram, V., Yazar, B., Ghobadi, S. & Gürsel, S. A. Development of graphene supported platinum nanoparticles for polymer electrolyte membrane fuel cells: Effect of support type and impregnation-reduction methods. *Int. J. Hydrogen Energy* **41**, 3414–3427 (2016).
76. Shinozaki, K., Zack, J. W., Richards, R. M., Pivovar, B. S. & Kocha, S. S. Oxygen Reduction Reaction Measurements on Platinum Electrocatalysts Utilizing Rotating Disk Electrode Technique. *J. Electrochem. Soc.* **162**, F1144–F1158 (2015).
77. Kim, D., Kim, D. W., Hong, W. G. & Coskun, A. Graphene/ZIF-8 composites with tunable hierarchical porosity and electrical conductivity. *J. Mater. Chem. A* **4**, 7710–7717 (2016).
78. Brunauer, S., Emmett, P. H. & Teller, E. Adsorption of Gases in Multimolecular Layers. *J. Am. Chem. Soc.* **60**, 309–319 (1938).
79. Sing, K. S. W. & Williams, R. T. Physisorption Hysteresis Loops and the

- Characterization of Nanoporous Materials. *Adsorpt. Sci. Technol.* **22**, 773–782 (2004).
80. Thommes, M. *et al.* Physisorption of gases, with special reference to the evaluation of surface area and pore size distribution (IUPAC Technical Report). *Pure Appl. Chem.* **87**, 1051–1069 (2015).
  81. Xu, C., Wang, X. & Zhu, J. Graphene–Metal Particle Nanocomposites. *J. Phys. Chem. C* **112**, 19841–19845 (2008).
  82. Sundaram, R. S., Gómez-Navarro, C., Balasubramanian, K., Burghard, M. & Kern, K. Electrochemical modification of grapheme. *Adv. Mater.* **20**, 3050–3053 (2008).
  83. Cui, X., Guo, L., Cui, F., He, Q. & Shi, J. Electrocatalytic Activity and CO Tolerance Properties of Mesostructured Pt/WO<sub>3</sub> Composite as an Anode Catalyst for PEMFCs. *J. Phys. Chem. C* **113**, 4134–4138 (2009).
  84. Zhou, H. *et al.* Spillover enhanced hydrogen storage in Pt-doped MOF/graphene oxide composite produced via an impregnation method. *Inorg. Chem. Commun.* **54**, 54–56 (2015).